Universal fractal structures in the weak interaction of solitary waves in generalized nonlinear Schrödinger equations

Yi Zhu[*]

Zhou Pei-Yuan Center for Applied Mathematics, Tsinghua University, Beijing 100084, People's Republic of China

Jianke Yang[†]

Department of Mathematics and Statistics, University of Vermont, 16 Colchester Avenue, Burlington, Vermont 05401, USA

Weak interactions of solitary waves in the generalized nonlinear Schrödinger equations are studied. It is first shown that these interactions exhibit similar fractal dependence on initial conditions for different nonlinearities. Then by using the Karpman-Solov'ev method, a universal system of dynamical equations is derived for the velocities, amplitudes, positions, and phases of interacting solitary waves. These dynamical equations contain a single parameter, which accounts for the different forms of nonlinearity. When this parameter is zero, these dynamical equations are integrable, and the exact analytical solutions are derived. When this parameter is nonzero, the dynamical equations exhibit fractal structures which match those in the original wave equations both qualitatively and quantitatively. Thus the universal nature of fractal structures in the weak interaction of solitary waves is analytically established. The origin of these fractal structures is also explored. It is shown that these structures bifurcate from the initial conditions where the solutions of the integrable dynamical equations develop finite-time singularities. Based on this observation, an analytical criterion for the existence and locations of fractal structures is obtained. Lastly, these analytical results are applied to the generalized nonlinear Schrödinger equations with various nonlinearities such as the saturable nonlinearity, and predictions on their weak interactions of solitary waves are made.

I. INTRODUCTION

Solitary wave interactions are a fascinating and important phenomenon for both physical and mathematical reasons. Physically, such interactions have arisen in a wide array of disciplines such as water waves [1], optics [2–7], and Josephson junctions [8]. For instance, in soliton-based fiber communication systems, optical pulses traveling in different frequency channels pass through each other, giving rise to collisions (strong interactions) of solitary waves. In the same frequency channel, neighboring optical pulses interfere with each other through overlapping tails, giving rise to weak interactions of solitary waves. Motivated by these physical applications, solitary wave interactions have been studied extensively in both the mathematical and physical communities. If the system is integrable, collisions of solitons are elastic [1], and weak interactions of solitons exhibit interesting yet simple behaviors [2,9–12]. However, in nonintegrable systems, solitary wave interactions can be far more complex. The first sign of this complexity was reported by Ablowitz *et al.* [13] for kink and antikink collisions in the ϕ^4 model where, inside the trapping interval, a reflection window was found. Later extensive numerical studies on this model by Campbell *et al.* [14–17] revealed that in fact, sequences of two- and more-bounce reflection windows exist, and the physical mechanism for these reflection windows is a resonant energy transfer between the translational motion and internal modes of kinks/antikinks. Anninos *et al.* [18]

pointed out further that there is a fractal structure in kink-antikink collisions. Using a collective-coordinate (i.e., variational) approach, they derived a set of fourth-order ordinary differential equations (ODEs) for these collisions, and these ODEs exhibit qualitatively similar fractal structures as in the ϕ^4 model (a comprehensive review on kink-antikink collisions in ϕ^4-type equations can be found in [19]). These complex dynamics turn out to be not restricted to kink-antikink collisions. Indeed, similar phenomena have been reported on kink-defect collisions in the sine-Gordon and ϕ^4 models [20–22], as well as vector-soliton collisions in the coupled nonlinear Schrödinger (NLS) equations [23–25]. Furthermore, fractal scattering has also been reported on weak interactions of breathers in a weakly discrete sine-Gordon equation [26] and weak interactions of solitary waves in a weakly discrete NLS equation [27]. Recently, Goodman and Haberman [28–30] provided a deep analysis on the collective-coordinate models (ODEs) for kink-antikink collisions in the ϕ^4 model [18], kink-defect collisions in the sine-Gordon model [20], and vector-soliton collisions in the coupled NLS equations [25,31] using sophisticated dynamical system techniques. They derived analytical formulas for the locations of reflection-window sequences, which agree qualitatively with numerical results on the original partial differential equations (PDEs). Their results shed much light on the origins of these window sequences and fractal structures, especially from a mathematical point of view.

Despite the above progress on solitary wave interactions, our understanding of these phenomena is far from satisfactory. On the collision of solitary waves, the analyses done so far were all based on approximate collective-coordinate approaches, hence the reduced ODE models can only provide

---

[*]Electronic address: zhuyi03@mails.tsinghua.edu.cn

[†]Electronic address: jyang@cems.uvm.edu

qualitative results at best. Many features reported in the ODE models cannot be seen in the PDE simulations, thus it is not possible to make a reliable prediction on the collision dynamics based on those ODE models and their analysis. In addition, the ODE models obtained from the collective-coordinate approaches not only are complicated, but also differ significantly from one PDE system to another. This forced previous researchers to analyze each PDE and its reduced ODE systems on an individual basis, which prevents an overall understanding on collision processes of solitary waves. On the weak interaction of solitary waves, the situation is even less satisfactory. The fractal nature of this weak interaction was reported only for systems which are weakly perturbed integrable systems (sine-Gordon and NLS equations, to be more specific) [26,27]. It is not known yet whether similar phenomena arise in strongly nonintegrable equations. More seriously, the previous work on this subject is largely numerical. No analysis has been attempted yet (not even the approximate collective-coordinate studies). Thus an analytical understanding of weak interactions of solitary waves is a completely open question.

In this paper, we study weak interactions of solitary waves in a whole class of generalized NLS equations (with arbitrary nonlinearities) both analytically and numerically. These generalized NLS equations are not weak perturbations of the NLS equation in general. First we show by direct PDE simulations that these weak interactions for different nonlinearities exhibit similar fractal structures on initial parameters of solitary waves. This establishes that fractal scattering is a common feature of weak interactions in this class of generalized NLS equations. Next, we rigorously derive a universal system of dynamical equations (ODEs) for the velocities, amplitudes, positions, and phases of interacting solitary waves in this class of PDEs by the Karpman-Solov'ev method. This universal ODE system is remarkably simple, and it contains only a single parameter which depends on the individual PDEs (after variable rescalings). When this parameter is zero, these dynamical equations are integrable, and their exact analytical solutions are derived. When this parameter is nonzero, the dynamical equations are found to exhibit fractal structures for a wide range of initial conditions. These fractal structures match those in the original PDEs both qualitatively and quantitatively, thus the universal nature of fractal scattering in the weak interaction of solitary waves is analytically established. We further explore the origin of these fractal structures. Our numerical studies on the ODE system show that these fractal structures bifurcate from the initial conditions where the solutions of the integrable dynamical equations develop finite-time singularities. Based on this observation, we present an analytical criterion for the existence and locations of fractal structures. One corollary from this criterion is that when the initial separation velocity is above a certain threshold value, fractal structures should disappear—a prediction which agrees with our PDE numerics as well as previous numerics on the weakly discrete NLS equation (see Fig. 6 in Ref. [27]). Lastly, we apply these analytical results to the generalized NLS equations with various nonlinearities such as the cubic-quintic, exponential, and saturable nonlinearities, and make detailed predictions on the dynamics of their weak interactions.

This paper is structured as follows. In Sec. II, we describe individual solitary waves in the generalized NLS equations. In Sec. III, we present direct PDE simulation results on weak interactions of solitary waves in the generalized NLS equations with two different nonlinearities, and reveal the common (universal) fractal structures in this class of PDEs. In Sec. IV, we analytically derive a universal system of dynamical equations (ODEs) for parameters of interacting solitary waves using asymptotic methods, and show that these ODEs accurately describe the weak interactions in the PDEs. In Sec. V, we solve this ODE system analytically when the single parameter in this system is equal to zero (which is the integrable case). In addition, we derive explicit conditions for the solutions of the integrable ODE system to develop finite-time singularities. In Sec. VI, we show that fractal structures appear in this ODE system when its parameter is nonzero and explore the origin of these fractal structures. In Sec. VII, we apply the analytical results to the generalized NLS equations with various nonlinearities. In Sec. VIII, we summarize the results of the paper and make some further remarks.

II. PRELIMINARIES

The generalized NLS equation is

$$iU_t + U_{xx} + F(|U|^2)U = 0, \qquad (2.1)$$

where $F(\cdot)$ is a real-valued algebraic function with $F(0)=0$. Equation (2.1) supports solitary waves of the form

$$U = \Phi(x - Vt - x_0; \beta)e^{1/2iV(x-x_0)-1/4iV^2t+i\beta t-i\sigma_0}, \qquad (2.2)$$

where $\Phi(\theta)$ is a positive function which satisfies the following equation:

$$\Phi_{\theta\theta} + F(|\Phi|^2)\Phi - \beta\Phi = 0,$$

$$\Phi \to 0, \quad |\theta| \to \infty, \qquad (2.3)$$

and $\beta(>0)$, V, x_0, and σ_0 are real constants. For convenience, we introduce the notations

$$\xi = Vt + x_0, \quad \theta = x - \xi,$$

$$\sigma = \left(\beta + \frac{1}{4}V^2\right)t - \sigma_0, \quad \phi = \frac{1}{2}V\theta + \sigma. \qquad (2.4)$$

Physically, β is the propagation constant which is related to the solitary-wave amplitude (henceforth, we call β an amplitude parameter), ϕ is the phase of the solitary wave, σ_0 is its initial phase, ξ is its center position, V is its velocity, and x_0 is its initial position. The solitary wave is characterized uniquely by its four parameters: V, β, σ_0, and and x_0. The asymptotic behavior of this solution at infinity is

$$\Phi(\theta) \to ce^{-\sqrt{\beta}|\theta|}, \quad |\theta| \to \infty, \qquad (2.5)$$

where c is the tail coefficient which is determined by the nonlinear function F and propagation constant β. We define the power of the solitary wave as

$$P(\beta) = \int_{-\infty}^{\infty} \Phi^2(\theta;\beta)d\theta, \qquad (2.6)$$

which plays an important role in the linear stability of the solitary wave. For general functions F, the analytical formulas for Φ, P, and c are not available; but for some special nonlinearities, one can find the analytical solutions. For instance, for the cubic-quintic nonlinearity

$$F(|U|^2) = \alpha|U|^2 + \gamma|U|^4, \qquad (2.7)$$

the analytical formulas for Φ, P, and c are [6,32]

$$\Phi(\theta;\beta) = \sqrt{\frac{4B\beta/\alpha}{B + \cosh 2\sqrt{\beta}\theta}}, \qquad (2.8)$$

$$P = \frac{4B\sqrt{\beta}\left(\pi/2 - \arctan\dfrac{B}{\sqrt{1-B^2}} \right)}{\alpha\sqrt{1-B^2}}, \qquad (2.9)$$

$$c = \sqrt{8B\beta/\alpha}, \qquad (2.10)$$

where

$$B = \text{sgn}(\alpha)\left(1 + \frac{16\beta\gamma}{3\alpha^2} \right)^{-1/2}. \qquad (2.11)$$

For special values of $\alpha=1$, $\gamma=0$, Eq. (2.1) becomes the integrable NLS equation, and then

$$B = 1, \quad \Phi(\theta;\beta) = \sqrt{2\beta}\,\text{sech}(\sqrt{\beta}\theta),$$

$$P = 4\sqrt{\beta}, \quad c = \sqrt{8\beta}. \qquad (2.12)$$

III. UNIVERSAL FRACTAL STRUCTURES IN WEAK INTERACTIONS OF SOLITARY WAVES

When two solitary waves are placed adjacent to each other, they would interfere through tail overlapping. In this case, the initial condition is

$$U(x,0) = U_1(x,0) + U_2(x,0),$$

$$U_k(x,0) = \Phi(x - x_{0,k};\beta_{0,k})e^{i\phi_{0,k}},$$

$$\phi_{0,k} = \frac{1}{2}V_{0,k}(x - x_{0,k}) - \sigma_{0,k}, \qquad (3.1)$$

where Φ satisfies Eq. (2.3). Here "0" in the subscript represents the initial value of the underlying parameter. For convenience, we assign the left solitary wave with index $k=1$, and the right solitary wave with index $k=2$. To study the weak interaction between these two solitary waves, we require that the two solitary waves are both stable, well-separated, and having almost the same velocities and amplitudes. Introducing notations

$$\beta = \frac{1}{2}(\beta_1 + \beta_2), \quad V = \frac{1}{2}(V_1 + V_2), \quad \xi = \frac{1}{2}(\xi_1 + \xi_2),$$

$$(3.2)$$

and

$$\Delta\beta = \beta_2 - \beta_1, \quad \Delta V = V_2 - V_1, \quad \Delta\xi = \xi_2 - \xi_1, \quad (3.3)$$

the above requirements then amount to

$$P_\beta > 0, \quad |\Delta\beta| \ll \beta, \quad |\Delta V| \ll 1, \quad \beta\Delta\xi \gg 1 \gg |\Delta\beta\Delta\xi|.$$

$$(3.4)$$

Here, $P_\beta \equiv dP/d\beta > 0$ corresponds to the Vakhitov-Kolokolov criterion for the linear stability of solitary waves in Eq. (2.1) [6,13].

Below, we numerically study the weak interaction of solitary waves in Eq. (2.1). This equation is numerically integrated by the pseudospectral method coupled with the fourth-order Runge-Kutta integration along the time direction. Since each solitary wave has four parameters, we have eight parameters in the initial conditions. Due to the phase, translation, and Galilean invariances of Eq. (2.1), we can fix $\sigma_{0,1}=0$, $x_{0,1}+x_{0,2}=0$, and $V_0 \equiv (V_{0,1}+V_{0,2})/2=0$ without any loss of generality. Also, for simplicity, we take $\Delta V_0 = V_{0,2} - V_{0,1}=0$ in all our simulations of this section, i.e., the two solitary waves are initially at rest. This leaves four free parameters in the initial conditions (3.1): $\Delta x_0 \equiv x_{0,2}-x_{0,1}$, $\Delta\phi_0 \equiv \phi_{0,2}-\phi_{0,1}=-\sigma_{0,2}$, $\beta_0 \equiv (\beta_{0,1}+\beta_{0,2})/2$, and $\Delta\beta_0 \equiv \beta_{0,2} - \beta_{0,1}$. We define the exit velocity $\Delta V_\infty \equiv \lim_{t\to+\infty} \Delta V$. We also define the collision time $\tilde{t}$ as the time when the two solitary waves are the closest (i.e., the separation distance between peaks of the two solitary waves is the smallest) during interactions. The lifetime of interaction is defined as the time length from the beginning $(t=0)$ to the collision time $\tilde{t}$, which is equal to the collision time in value. Thus $\tilde{t}$ will be used to denote the lifetime as well. Of the four parameters in initial conditions, we will fix β_0, $\Delta\beta_0$, and Δx_0, and use $\Delta\phi_0$ as the control parameter and vary it continuously between 0 and 2π. At each $\Delta\phi_0$ value, we simulate the evolution of the two solitary waves and record the exit velocity and the lifetime. Numerically, the exit velocity is determined as follows. We let the solitary waves propagate for a long time. If they still do not separate, we assign the exit velocity as zero. If they do separate, we wait until they have separated far apart and their velocities stabilized. Then we locate the positions of maximum solitary wave amplitudes at serval different time values. The average separation velocity of the two solitary waves in these time intervals is assigned as the exit velocity. The numerical lifetime is simply the time when the two solitary waves are the closest in the simulations. Below, we carry out numerical studies of weak interactions as described above on two different nonlinearities: the cubic-quintic and exponential nonlinearities.

A. Weak interactions for the cubic-quintic nonlinearity

Our first example of nonlinearity is the cubic-quintic nonlinearity (2.7), which arises in a wide array of physical systems such as optics [6] and boson condensates [32,34]. In this nonlinearity, we set

$$\alpha = 1, \quad \gamma = 0.04. \qquad (3.5)$$

It is easy to verify that all solitary waves [Eq. (2.8)] in this case are linearly stable using the Vakhitov-Kolokolov criterion. In our simulations, we set $\Delta x_0=10$ and $\beta_0=1$. The x

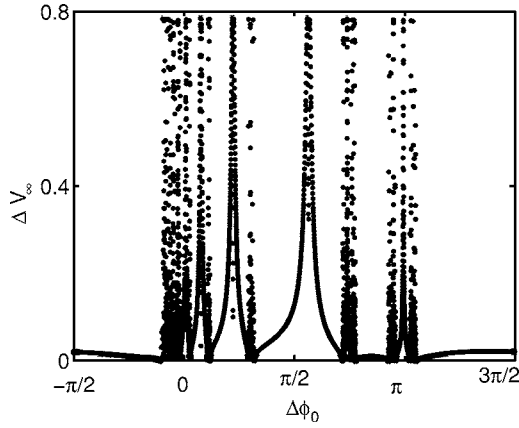FIG. 1. The graph of exit velocity ΔV_∞ versus the initial phase difference $\Delta\phi_0$ in the nonequal initial amplitude case of the cubic-quintic NLS equations (2.1) and (2.7). The cubic and quintic nonlinearity coefficients are given in Eq. (3.5), and the other (fixed) initial parameters are $\Delta x_0=10$, $\beta_0=1$, $\Delta\beta_0=-0.065$, and $\Delta V_0=0$.

interval is 70 units wide, discretized by 512 grid points; and the time step size is 0.004.

We first study the nonequal-amplitude case and take $\Delta\beta_0=-0.065$. The ΔV_∞ versus $\Delta\phi_0$ diagram is shown in Fig. 1. The prominent structures in this graph can be split into two regions: one region is $-0.34<\Delta\phi_0<2.5$ and the other region is $2.9<\Delta\phi_0<3.3$. The structures in these two regions turn out to be quite similar (except a horizontal reflection with respect to a vertical axis), thus we focus on the larger region $-0.34<\Delta\phi_0<2.5$ below. The main structure in this region forms a sequence of hills; their widths get smaller from the right to the left, and their heights are about the same. These hills will be called the primary hills. This primary-hill sequence converges to the accumulation point $\Delta\phi_{0c}=-0.339$. In order to see this hill sequence near the accumulation point $\Delta\phi_{0c}$ more clearly, we zoom in on the region $[-0.35,0.4]$, and the zoomed-in diagram is shown in Fig. 2. In this figure, the cascading sequence can be seen very clearly [see Fig. 2(a)]. In Fig. 2(b), the corresponding lifetime diagram is displayed. We can see that on the same hill, interactions have roughly the same lifetime. On different hills, lifetimes are different: hills closer to the accumulation point $\Delta\phi_{0c}$ have longer lifetimes. Between hills, even longer lifetimes can be seen, suggesting more complex dynamics there. To explore differences in interaction dynamics on different hills, we select three points, $\Delta\phi_0=0.1759$, -0.0057, and -0.1053 [marked in Fig. 2(a) by circles], on three adjacent primary hills. These points are at the same relative positions (roughly halfway between the peak and bottom) of the respective hills. At these points, the interaction dynamics is plotted in Figs. 2(1–3). Here only the separation distance $\Delta\xi$ versus time t graphs are shown. We find that these three dynamical processes are similar, except that the oscillation times before final separation differ by one from one hill to the next. The lifetimes $\tilde{t}_n$ of interactions on this primary hill sequence are found to be an almost perfect linear function of the hill index n as

$$\omega\tilde{t}_n = 2n\pi + \delta, \tag{3.6}$$
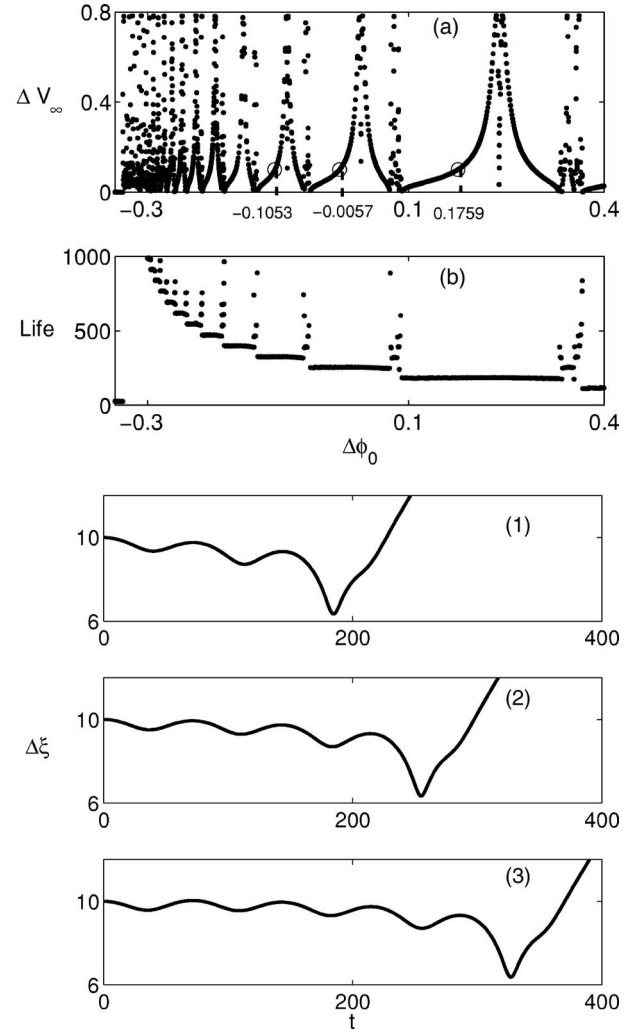
where the least-squares linear fit gives

FIG. 2. (a) The exit velocity versus initial phase difference graph of Fig. 1 replotted near the accumulation point of the primary hill sequence; (b) the lifetime versus initial phase difference graph; and (1)–(3): separation versus time diagrams of solitary wave interactions at three values of $\Delta\phi_0$ marked by circles in (a): (1) 0.1759; (2) -0.0057; and (3) -0.1053.

$$\omega = 0.08605, \quad \delta = 2.8897. \tag{3.7}$$

Here the lifetime of each primary hill is measured numerically at the relative location of that hill shown in Fig. 2(a) by circles. This lifetime formula has the same form as those for all window sequences reported before [15,16,20,23,29].

In addition to the primary hill sequence as described above, Fig. 1 also possesses higher-order structures between primary hills. To demonstrate, we first isolate the long interval $[-0.35,2.5]$ in Fig. 1 and replot that part of the graph in Fig. 3(a). Then we zoom into its subinterval [0.91, 0.995], which is between the two largest primary hills in Fig. 3(a). The zoomed-in graph is shown in Fig. 3(b). We see that the zoomed-in graph is similar to Fig. 3(a), but the cascading direction has reversed. This behavior is analogous to that reported in [18,24] for the ϕ^4 model and the coupled NLS equations. The main structure in this zoomed-in window is again two sequences of hills, accumulating to the left and
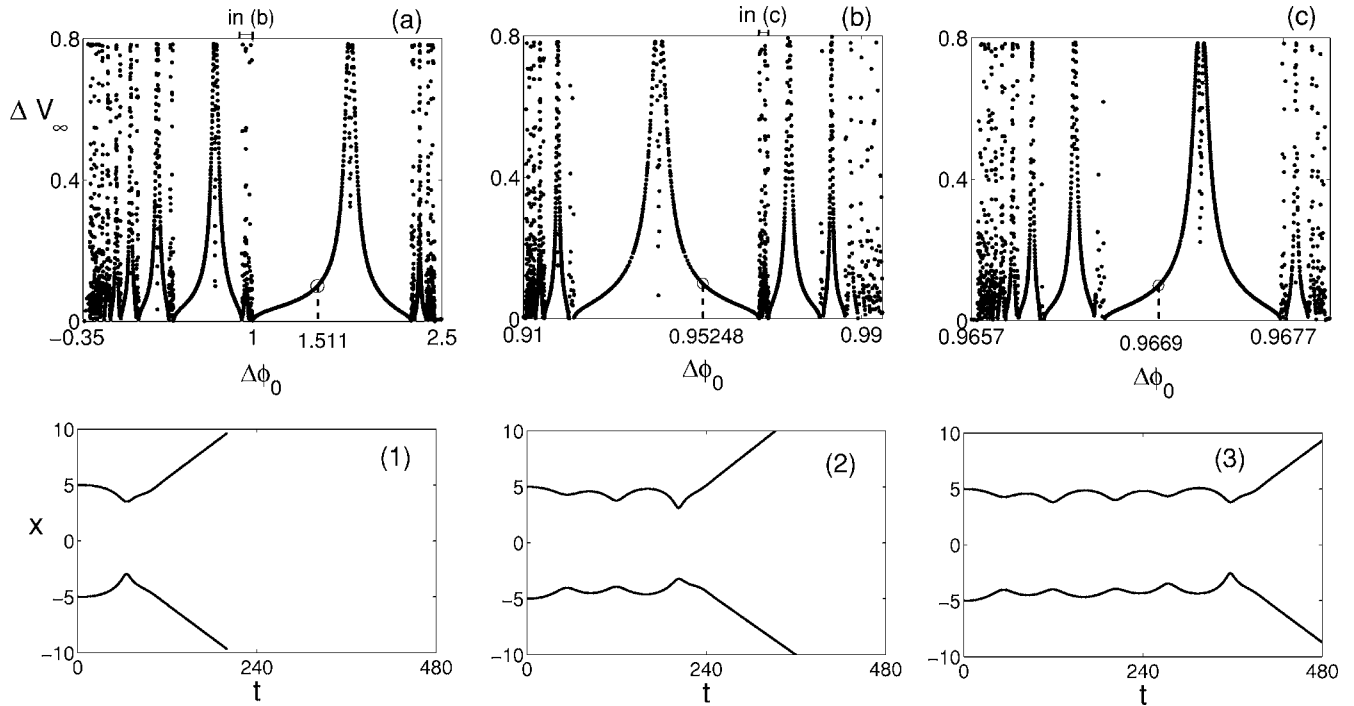
FIG. 3. Top: the exit velocity versus initial phase difference graph of Fig. 1 and its two zoomed-in structures; bottom: soliton-positions versus time diagrams at three values of $\Delta\phi_0$ marked by circles in the top panel: (1) 1.511; (2) 0.95248; and (3) 0.9669.

right, respectively. We call them secondary hills. Between secondary hills, we see even higher-order structures. To see these structures more clearly, we zoom into the subinterval [0.9657, 0.96785], which is between the two largest secondary hills in Fig. 3(b). The zoomed-in graph is shown in Fig. 3(c). We see that it is again similar to Fig. 3(b) but with a reversed cascading direction. One can zoom into the regions between these tertiary hills in Fig. 3(c) further, and will get even higher order structures which are similar to the ones shown in Fig. 3. Thus Fig. 3(a) is a fractal structure. We have also explored the interaction dynamics on this fractal. To demonstrate, we pick three $\Delta\phi_0$ values 1.511, 0.952 48, and 0.9669 which are at the same relative positions of the fractal (roughly halfway between the peak and bottom of the widest hills) in Figs. 3(a)–3(c) (marked by circles). The interaction dynamics at these three points are displayed in Figs. 3(1–3), respectively. Here the positions of maximum amplitudes of the interacting waves are plotted against time. We see that these dynamical patterns are clearly similar, except that the numbers of oscillations before final separation are different.

In the above numerical simulations, the two solitary waves have different initial amplitudes ($\Delta\beta_0 = -0.065$). We have also studied interactions of equal-amplitude solitary waves, i.e., with $\Delta\beta_0 = 0$, while keeping the other parameters the same. In this case, the graph of exit velocity ΔV_∞ versus initial phase difference $\Delta\phi_0$ is shown in Fig. 4. This graph is symmetric with respect to $\Delta\phi_0$ for obvious reasons. Examination of this graph shows that it is also a fractal. Thus fractal dependence arises in weak interactions of both equal and nonequal amplitude solitary waves.

B. Weak interactions with exponential nonlinearity

To explore whether the above fractal structures for weak interactions persist or not with other types of nonlinearities,

we consider in this section a different type of nonlinearity, the exponential nonlinearity, with

$$F(|U|^2) = e^{|U|} - 1. \tag{3.8}$$

Here, -1 is introduced into this function to meet the condition $F(0) = 0$. Note that this nonlinearity does not have any parameters. Throughout this section, we set the initial separation $\Delta x_0 = 8$, and average propagation constant $\beta_0 = 2.3$. We study two cases, one for nonequal amplitudes with $\Delta\beta_0 = -0.045$, and the other for equal amplitudes with $\Delta\beta_0 = 0$.
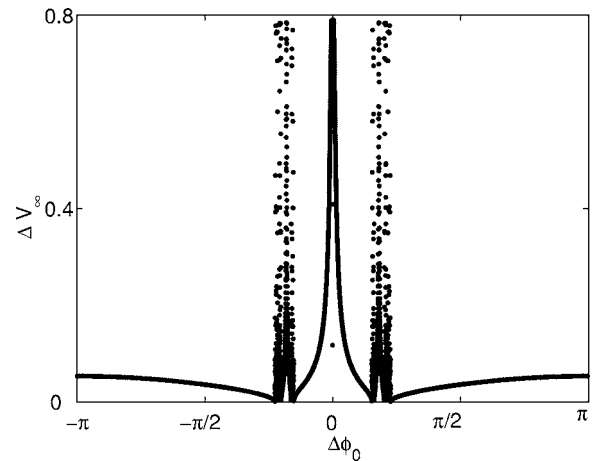

FIG. 4. The exit velocity versus initial phase difference graph in the equal initial amplitude case of the cubic-quintic NLS equations (2.1) and (2.7). The cubic and quintic nonlinearity coefficients as well as the initial conditions are the same as in Fig. 1, except that $\Delta\beta_0 = 0$ now.
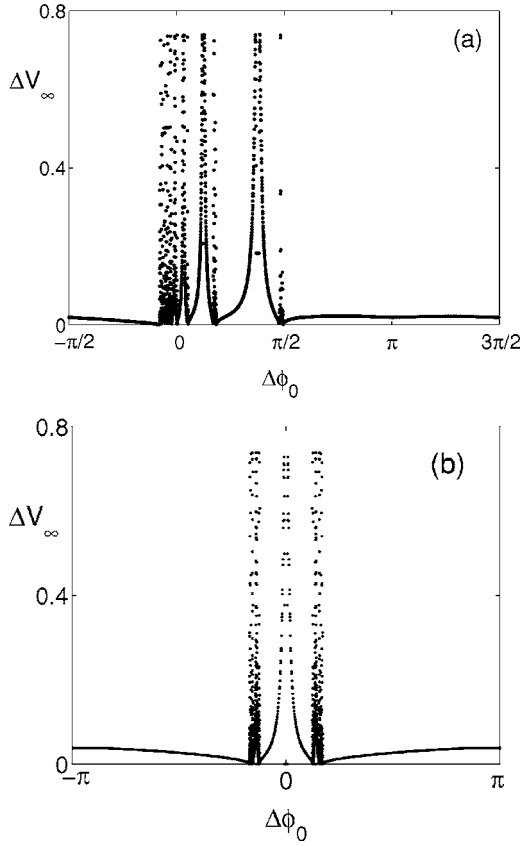
FIG. 5. The exit velocity versus initial phase difference graphs for the exponential nonlinearity (3.8): (a) the nonequal initial amplitude case with $\Delta\beta_0 = -0.045$ and (b) the equal initial amplitude case with $\Delta\beta_0 = 0$. The other (fixed) initial parameters are $\beta_0 = 2.3$, $\Delta x_0 = 8$, and $\Delta V_0 = 0$.

For both cases, the control parameter is $\Delta\phi_0$ as before. In our simulations, the x interval was 70 units wide, discretized by 512 grid points. The time step size was 0.002. The ΔV_∞ versus $\Delta\phi_0$ graphs for both cases are plotted in Fig. 5. We have verified that both graphs in this figure are fractals. Comparing these fractals with those in Figs. 1 and 4 of the cubic-quintic nonlinearity, we see that the fractal structures for these two different nonlinearities are very similar. The only major difference between them is in the nonequal amplitude case, where there is only one primary hill sequence (accumulating toward the left) for the exponential nonlinearity, while there are two primary hill sequences for the cubic-quintic nonlinearity. It is remarkable that two very different nonlinearities exhibit quite similar fractal dependence on initial conditions. Thus fractal scattering appears to be a universal feature in weak interactions of Eq. (2.1) rather than an accident. This leads us to the following questions: how can we analytically establish the universal nature of fractal scatterings for Eq. (2.1) with general nonlinearities? How can we analytically explain the major differences of fractals for different nonlinearities? These questions will be answered in the following sections.

IV. DYNAMICAL EQUATIONS

To study weak interactions analytically, we use the Karpman-Solov'ev method [9] by treating the interference as a small perturbation to each solitary wave (see also [35]). This method has been successfully used before on the NLS equation [2,9,10,35], the modified NLS equation [11], the Manakov equations [12], as well as the (nonintegrable) coupled NLS equations [36]. To proceed, we first need to consider the evolution of a single solitary wave in the perturbed generalized NLS equation

$$iU_t + U_{xx} + F(|U|^2)U = \epsilon G, \tag{4.1}$$

where function G is a perturbation term, and ϵ is a small parameter. Without perturbations ($\epsilon = 0$), the solitary wave [Eq. (2.2)] is an exact solution of Eq. (4.1), and its internal parameters V, β, σ_0, and x_0 are time-independent. When the perturbation is turned on, these internal parameters of the solitary wave will evolve slowly on the time scale $T = \epsilon t$. The multiple-scale perturbation theory for this slow evolution is well-known [36,37]. We write the perturbed solution as

$$U = \hat{\Phi}(\theta, t, T)e^{iV\theta/2 + i\sigma}, \tag{4.2}$$

where

$$\theta = x - \int_0^t V dt - x_0, \quad \sigma = \int_0^t (\beta + V^2/4)dt - \sigma_0. \tag{4.3}$$

Here $V(T)$, $\beta(T)$, $\sigma_0(T)$, and $x_0(T)$ are all functions of slow time T. Next, we will derive the dynamical equations (ODEs) for the slow-time evolution of these parameters. Substituting Eq. (4.2) into Eq. (4.1), we get the equation for $\hat{\Phi}$ as

$$i\hat{\Phi}_t + \hat{\Phi}_{\theta\theta} - \beta\hat{\Phi} + F(\hat{\Phi}^2)\hat{\Phi} = \epsilon Ge^{-i\phi} - \epsilon[i\hat{\Phi}_\beta\beta_T - i\hat{\Phi}_\theta x_{0T}]$$
$$- \epsilon(Vx_{0T}/2 - V_T\theta/2 + \sigma_{0T})\hat{\Phi}, \tag{4.4}$$

where ϕ is defined in Eq. (2.4). We expand the amplitude function $\hat{\Phi}$ into a perturbation series

$$\hat{\Phi} = \Phi(\theta; \beta) + \epsilon\tilde{\Phi} + O(\epsilon^2). \tag{4.5}$$

The equation at order ϵ^0 is satisfied automatically since Φ satisfies Eq. (2.3). At order ϵ, the equation for $\tilde{\Phi}$ can be written as

$$i\Psi_t + \mathcal{L}\Psi = H, \tag{4.6}$$

where

$$\Psi = \begin{pmatrix} \tilde{\Phi} + \tilde{\Phi}^* \\ \tilde{\Phi}^* - \tilde{\Phi} \end{pmatrix}, \quad \mathcal{L} = \begin{pmatrix} 0 & \mathcal{L}_0 \\ \mathcal{L}_1 & 0 \end{pmatrix}, \tag{4.7}$$

$$\mathcal{L}_0 = -\partial_{\theta\theta} + \beta - F(\Phi^2),$$

$$\mathcal{L}_1 = -\partial_{\theta\theta} + \beta - F(\Phi^2) - 2\Phi^2 F'(\Phi^2), \tag{4.8}$$

and

$$H = \begin{bmatrix} -G^*e^{i\phi} + Ge^{-i\phi} - 2i\Phi_\beta\beta_T + 2i\Phi_\theta x_{0T} \\ -G^*e^{i\phi} - Ge^{-i\phi} + (Vx_{0T} - \theta V_T + 2\sigma_{0T})\Phi \end{bmatrix}. \tag{4.9}$$

Here the superscript asterisk represents complex conjugation. Operator $\mathcal{L}$ has two eigenfunctions and two generalized

eigenfunctions associated with the zero eigenvalue,

$$\Psi_1 = \begin{pmatrix} \Phi_\theta \\ 0 \end{pmatrix}, \quad \Psi_2 = \begin{pmatrix} 0 \\ \Phi \end{pmatrix},$$

$$\widetilde{\Psi}_1 = \begin{pmatrix} 0 \\ -\theta\Phi/2 \end{pmatrix}, \quad \widetilde{\Psi}_2 = \begin{pmatrix} -\Phi_\beta \\ 0 \end{pmatrix}, \qquad (4.10)$$

with the relations

$$\mathcal{L}\Psi_k = 0, \quad \mathcal{L}\widetilde{\Psi}_k = \Psi_k, \quad k = 1,2. \qquad (4.11)$$

In order for the inhomogeneous solution Ψ of the first-order equation (4.6) to be nonsecular at large time, the inhomogeneous term in Eq. (4.6) must be orthogonal to the above eigenfunctions and generalized eigenfunctions of the zero eigenvalue, i.e.,

$$\langle H, \Psi_k \rangle = \langle H, \widetilde{\Psi}_k \rangle = 0, \quad k = 1,2, \qquad (4.12)$$

under the inner product defined as

$$\langle F_1, F_2 \rangle = \int_{-\infty}^{\infty} F_1^\dagger \begin{pmatrix} 0 & 1 \\ 1 & 0 \end{pmatrix} F_2 d\theta. \qquad (4.13)$$

Here $F_k^\dagger$ is the Hermitian of F_k. Evaluating the four integrals in Eq. (4.12), the slow-time evolution equations for parameters $V(T)$, $\beta(T)$, $\sigma_0(T)$, and $x_0(T)$ will be obtained. These evolution equations can be written as

$$P \frac{dV}{dT} = 2 \int_{-\infty}^{\infty} \Phi_\theta (G^* e^{i\phi} + G e^{-i\phi}) d\theta, \qquad (4.14)$$

$$P_\beta \frac{d\beta}{dT} = \frac{1}{i} \int_{-\infty}^{\infty} \Phi (G e^{-i\phi} - G^* e^{i\phi}) d\theta, \qquad (4.15)$$

$$P \frac{dx_0}{dT} = \frac{1}{i} \int_{-\infty}^{\infty} \Phi \theta (G e^{-i\phi} - G^* e^{i\phi}) d\theta, \qquad (4.16)$$

$$P_\beta \left(\frac{V}{2} \frac{dx_0}{dT} + \frac{d\sigma_0}{dT} \right) = \int_{-\infty}^{\infty} \Phi_\beta (G^* e^{i\phi} + G e^{-i\phi}) d\theta. \qquad (4.17)$$

These equations will be critical for the development of weak interaction theory of solitary waves below.

Now, we consider the weak interaction of two solitary waves. Here the tail overlapping can be considered as a small perturbation which causes the internal parameters of each solitary wave to evolve on a slow time scale ϵt. Here ϵ is the magnitude of tail overlapping which is exponentially small with solitary wave spacing $\Delta\xi$. We will not introduce ϵ explicitly in the next analysis. To the leading order, the interacting solution is simply a superposition of two solitary waves,

$$U = U_1 + U_2,$$

$$U_k = \Phi_k e^{i\phi_k}, \quad k = 1,2, \qquad (4.18)$$

where all parameters slowly vary over time. Picking up the dominant interference terms, each solitary wave is governed by the following perturbed generalized NLS equations:

$$iU_{k,t} + iU_{k,\theta\theta} + F(|U_k|^2) U_k = H_k, \qquad (4.19)$$

where

$$H_k = -[F(|U_k|^2) + F'(|U_k|^2)|U_k|^2] U_{3-k} - F'(|U_k|^2) U_k^2 U_{3-k}^*. \qquad (4.20)$$

In this paper, we only study the weak interaction, so conditions (3.4) are assumed. Since $|\Delta V| \ll 1$, the phase difference

$$\Delta\phi = \phi_2 - \phi_1 \approx -V\Delta\xi/2 + \Delta\sigma, \qquad (4.21)$$

which is independent of θ.

Now we apply the above solitary wave perturbation theory to Eq. (4.19). In this problem,

$$\epsilon G e^{-i\phi} = -[F(\Phi_k^2)\Phi_{3-k} + F'(\Phi_k^2)\Phi_k^2\Phi_{3-k}] e^{(-1)^{k+1} i\Delta\phi}$$
$$- F'(\Phi_k^2)\Phi_k^2\Phi_{3-k} e^{(-1)^k i\Delta\phi}. \qquad (4.22)$$

Substituting Eq. (4.22) into Eqs. (4.14)–(4.17), we obtain the following dynamical equations:

$$P_k \frac{dV_k}{dt} = -4 \int_{-\infty}^{\infty} \Phi_{k,\theta}[F(\Phi_k^2)\Phi_{3-k}$$
$$+ 2F'(\Phi_k^2)\Phi_k^2\Phi_{3-k}] d\theta \cos(\Delta\phi), \qquad (4.23)$$

$$P_{k,\beta_k} \frac{d\beta_k}{dt} = (-1)^k 2 \int_{-\infty}^{\infty} \Phi_k F(\Phi_k^2)\Phi_{3-k} d\theta \sin(\Delta\phi), \qquad (4.24)$$

$$P_k \frac{dx_{k,0}}{dt} = (-1)^k 2 \int_{-\infty}^{\infty} \Phi_k \theta F(\Phi_k^2)\Phi_{3-k} d\theta \sin(\Delta\phi), \qquad (4.25)$$

$$P_{k,\beta_k} \left(\frac{V_k}{2} \frac{dx_{k,0}}{dt} + \frac{d\sigma_{k,0}}{dt} \right) = -2 \int_{-\infty}^{\infty} \Phi_{k,\beta_k}[F(\Phi_k^2)\Phi_{3-k}$$
$$+ 2F'(\Phi_k^2)\Phi_k^2\Phi_{3-k}] d\theta \cos(\Delta\phi), \qquad (4.26)$$

where P_k, $k=1,2$ are powers of the two individual solitary waves. These equations can be simplified greatly. Due to assumptions (3.4), and noticing that $\Phi(\theta)$ and $\Phi_\beta(\theta)$ are even functions of θ, the leading-order terms of the above integrals can be explicitly calculated. For instance,

$$\int_{-\infty}^{\infty} \Phi_k F(\Phi_k^2)\Phi_{3-k}d\theta = \int_{-\infty}^{\infty} \Phi F(\Phi^2)ce^{(-1)^{k+1}\sqrt{\beta}\theta}d\theta e^{-\sqrt{\beta}\Delta\xi}$$

$$= \int_{-\infty}^{\infty} (\beta\Phi - \Phi_{\theta\theta})ce^{\sqrt{\beta}\theta}d\theta e^{-\sqrt{\beta}\Delta\xi}$$

$$= 2\sqrt{\beta}c^2 e^{-\sqrt{\beta}\Delta\xi}. \tag{4.27}$$

Similarly,

$$\int_{-\infty}^{\infty} \Phi_{k,\theta}[F(\Phi_k^2)\Phi_{3-k} + 2F'(\Phi_k^2)\Phi_k^2\Phi_{3-k}]d\theta$$

$$= \int_{-\infty}^{\infty} \Phi_\theta[F(\Phi^2) + 2F'(\Phi^2)\Phi^2]ce^{(-1)^{k+1}\sqrt{\beta}\theta}d\theta e^{-\sqrt{\beta}\Delta\xi}$$

$$= (-1)^k\sqrt{\beta}\int_{-\infty}^{\infty} \Phi F(\Phi^2)ce^{\sqrt{\beta}\theta}d\theta e^{-\sqrt{\beta}\Delta\xi}$$

$$= (-1)^k 2\beta c^2 e^{-\sqrt{\beta}\Delta\xi}, \tag{4.28}$$

$$\int_{-\infty}^{\infty} \Phi_k\theta F(\Phi_k^2)\Phi_{3-k}d\theta = \int_{-\infty}^{\infty} \Phi\theta F(\Phi^2)ce^{(-1)^{k+1}\sqrt{\beta}\theta}d\theta e^{-\sqrt{\beta}\Delta\xi}$$

$$= (-1)^{k+1}\int_{-\infty}^{\infty} \Phi\theta F(\Phi^2)ce^{\sqrt{\beta}\theta}d\theta e^{-\sqrt{\beta}\Delta\xi}$$

$$\overset{def}{=} (-1)^{k+1}D_1 e^{-\sqrt{\beta}\Delta\xi}, \tag{4.29}$$

$$\int_{-\infty}^{\infty} \Phi_{k,\beta_k}[F(\Phi_k^2)\Phi_{3-k} + 2F'(\Phi_k^2)\Phi_k^2\Phi_{3-k}]d\theta$$

$$= \int_{-\infty}^{\infty} \Phi_\beta[F(\Phi^2) + 2F'(\Phi^2)\Phi^2]ce^{(-1)^{k+1}\sqrt{\beta}\theta}d\theta e^{-\sqrt{\beta}\Delta\xi}$$

$$= \int_{-\infty}^{\infty} \Phi_\beta[F(\Phi^2) + 2F'(\Phi^2)\Phi^2]ce^{\sqrt{\beta}\theta}d\theta e^{-\sqrt{\beta}\Delta\xi}$$

$$\overset{def}{=} D_2 e^{-\sqrt{\beta}\Delta\xi}. \tag{4.30}$$

With the above simplifications, the dynamical equations reduce to

$$P\frac{dV_k}{dt} = (-1)^{k+1} 8\beta c^2 \cos(\Delta\phi)e^{-\sqrt{\beta}\Delta\xi}, \tag{4.31}$$

$$P_\beta\frac{d\beta_k}{dt} = (-1)^k 4\sqrt{\beta}c^2 \sin(\Delta\phi)e^{-\sqrt{\beta}\Delta\xi}, \tag{4.32}$$

$$P\frac{dx_{k,0}}{dt} = -2D_1 \sin(\Delta\phi)e^{-\sqrt{\beta}\Delta\xi}, \tag{4.33}$$

$$P_\beta\left(\frac{V}{2}\frac{dx_{k,0}}{dt} + \frac{d\sigma_{k,0}}{dt}\right) = -2D_2 \cos(\Delta\phi)e^{-\sqrt{\beta}\Delta\xi}, \tag{4.34}$$

where P is the power of the solitary wave with propagation constant β, and D_1, D_2 are defined in Eqs. (4.29) and (4.30). From the above equations, we find that

$$\beta_t = V_t = 0, \tag{4.35}$$

$$\Delta\xi_t = \Delta V, \tag{4.36}$$

$$\Delta\phi_t = \Delta\beta, \tag{4.37}$$

$$\Delta V_t = -\frac{16\beta c^2}{P}\cos(\Delta\phi)e^{-\sqrt{\beta}\Delta\xi}, \tag{4.38}$$

$$\Delta\beta_t = \frac{8\sqrt{\beta}c^2}{P_\beta}\sin(\Delta\phi)e^{-\sqrt{\beta}\Delta\xi}. \tag{4.39}$$

Equations (4.35)–(4.39) are the key results in the weak interaction theory of solitary waves. These equations can be further simplified by variable rescalings. Introducing notations

$$\psi = \Delta\phi, \quad \zeta = -\sqrt{\beta}\Delta\xi, \quad f = \frac{16\beta^{3/2}c^2}{P}, \quad g = \frac{8\sqrt{\beta}c^2}{P_\beta}, \tag{4.40}$$

and

$$\tau = \sqrt{f}t, \quad \varepsilon = \frac{g}{f} - 1 = \frac{P}{2\beta P_\beta} - 1, \tag{4.41}$$

then the dynamical equations (4.36)–(4.39) reduce to

$$\zeta_{\tau\tau} = \cos\psi e^\zeta,$$

$$\psi_{\tau\tau} = (1 + \varepsilon)\sin\psi e^\zeta. \tag{4.42}$$

Equation (4.42) is the final dynamical system we obtained for the analytical treatment of weak interactions in the generalized NLS equations (2.1). It is important to remark that Eq. (4.42) is universal for the generalized NLS equations with arbitrary nonlinearities. It contains only a single parameter ε, which depends on the specific form of nonlinearity.

Equation (4.42) has the following general properties. First, it is Hamiltonian with the conserved Hamiltonian (energy) as

$$E = \frac{1}{2}(\dot{\zeta}^2 - \dot{\psi}^2) - e^\zeta\cos\psi + \frac{\varepsilon}{2(1+\varepsilon)}\dot{\psi}^2. \tag{4.43}$$

Here $(\dot{\ }) \equiv d/d\tau$. Second, it has some symmetry properties. One is that it is time-reversible, i.e., if $[\zeta(\tau), \psi(\tau)]$ is a solution with initial conditions $(\zeta_0, \dot{\zeta}_0, \psi_0, \dot{\psi}_0)$, then $[\zeta(-\tau), \psi(-\tau)]$ is a solution with initial conditions $(\zeta_0, -\dot{\zeta}_0, \psi_0, -\dot{\psi}_0)$. Another symmetry is on phase flipping, i.e., if $[\zeta(\tau), \psi(\tau)]$ is a solution with initial conditions $(\zeta_0, \dot{\zeta}_0, \psi_0, \dot{\psi}_0)$, then $[\zeta(\tau), -\psi(\tau)]$ is a solution with initial conditions $(\zeta_0, \dot{\zeta}_0, -\psi_0, -\dot{\psi}_0)$. Physically, this latter symmetry corresponds to the interchange of the left and right solitary waves in the PDE evolutions, which of course does not change the interaction outcome. Equation (4.42) also has the property that if $\psi(\tau)$ is a solution, so is $\psi(\tau) + 2n\pi$ for any integer of n. This reflects the fact that in the PDE system, solution evolution remains the same if the phase difference between the solitary waves changes by a multiple of 2π.

The dynamical equations (4.42) are asymptotically accurate in describing weak interactions in the PDE system (to the leading order) when the spacing $\Delta\xi$ is large. Surprisingly, even when the two solitary waves come close to each other, Eq. (4.42) can still describe the interaction process very well. This is analogous to weak interactions in the (integrable) NLS equation [2,9]. Below, we make detailed comparisons between the ODE solutions of Eq. (4.42) and the PDE solutions in Sec. III A for the cubic-quintic nonlinearity. Inserting the parameter values $\alpha=1$, $\gamma=0.04$, and $\beta_0=1$ of PDE simulations into Eqs. (2.9) and (2.10), we get $P=3.747\,20$, $P_\beta=1.648\,35$, and $c=2.694\,95$, thus $f=31.010\,80$, $g=35.248\,45$, and $\varepsilon=0.136\,65$. Corresponding to the initial conditions for PDE simulations in Sec. III A, the initial conditions for the ODE system (4.42) with nonequal and equal initial amplitudes are

$$\zeta_0 = -10, \quad \dot{\zeta}_0 = 0, \quad \dot{\psi}_0 = -0.011\,67, \qquad (4.44)$$

and

$$\zeta_0 = -10, \quad \dot{\zeta}_0 = 0, \quad \dot{\psi}_0 = 0, \qquad (4.45)$$

respectively. In both cases, the initial phase difference ψ_0 is the control parameter as in PDE simulations. The ODE system (4.42) is numerically solved by the fourth-order Runge-Kutta method, with the time step set as 0.01. The simulation results on the exit velocity $-\dot{\zeta}_\infty$ versus ψ_0 graph are shown in Fig. 6. Clearly, these graphs are very similar to Figs. 1 and 4 from PDE simulations. We have also investigated the detailed structures of Fig. 6 in ways analogous to what we did for Figs. 2 and 3. Specifically, we have examined the primary hill sequence in Fig. 6(a) and zoomed into regions between primary hills. The results are shown in Figs. 7 and 8, respectively. Both figures closely resemble Figs. 2 and 3 from the PDE simulations.

The agreement between the ODE model and the PDE simulations is not only qualitative, but also quantitative. To demonstrate, we compare the locations and lifetimes of primary hill sequences in Figs. 2 and 7. The comparison results are summarized in Table I. Very good quantitative agreement between them can be seen. In the ODE model, the lifetime is also an almost perfect linear function of the hill index n in the form (3.6). When the time rescaling (4.41) is recovered, the ODE model gives

$$\omega|_{ODE} = 0.085\,70, \qquad \delta|_{ODE} = 2.9655, \qquad (4.46)$$

closely resembling the corresponding values (3.7) from the PDE simulations.

Above we have established that the reduced ODE system (4.42) accurately describes weak interactions of the PDE system. Since the ODE system (4.42) is universal for Eq. (2.1) regardless of details of its nonlinearities, we see that the hill sequences and fractal structures in Eq. (4.42) are universal for weak interactions of solitary waves in the PDE system (2.1), as Figs. 1 and 4–6 clearly indicate.
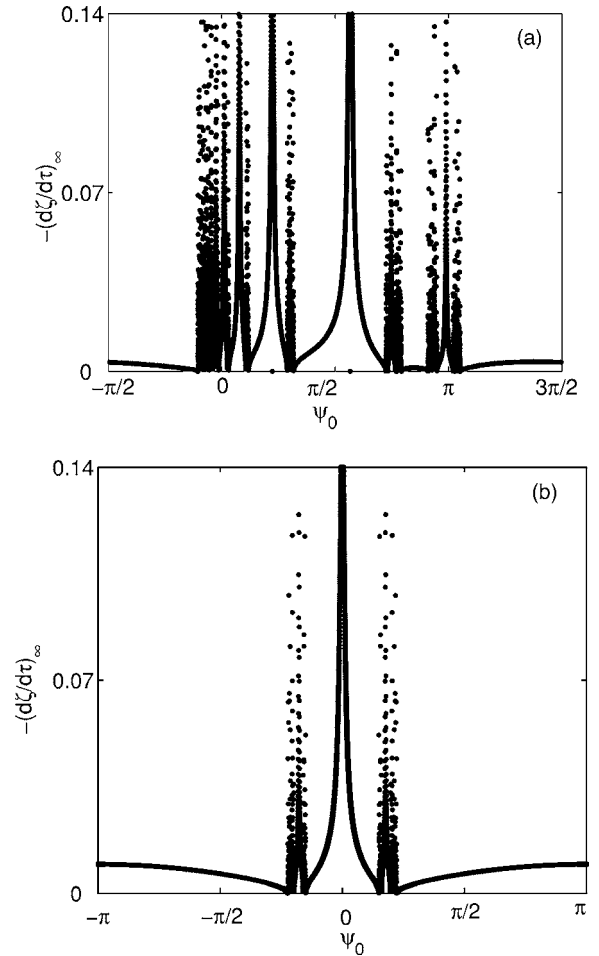

FIG. 6. The exit velocity $(-\dot{\zeta}_\infty)$ versus the initial phase difference (ψ_0) graphs from the ODE model (4.42). Here the initial conditions for (a) and (b) are chosen corresponding to the PDE simulation results in Figs. 1 and 4, respectively (see text).

Next we will turn our attention to the ODE system (4.42) and analyze its solution dynamics in more detail. In particular, we would like to understand why fractal structures arise in this system, and how to analytically predict their locations and other main features.

V. SOLUTIONS OF THE INTEGRABLE DYNAMICAL EQUATIONS AND THEIR SINGULARITY CONDITIONS

Equation (4.42) conserves energy [Eq. (4.43)] for all values of ε. When $\varepsilon=0$, it has another conserved quantity,

$$M = \dot{\zeta}\dot{\psi} - e^\zeta \sin\psi, \qquad (5.1)$$

which can be called the momentum of this system. In this particular case, system (4.42) is an integrable Hamiltonian system and can be analytically solved. Let $Y=\zeta+i\psi$, Eq. (4.42) becomes

$$Y_{\tau\tau} = e^Y. \qquad (5.2)$$

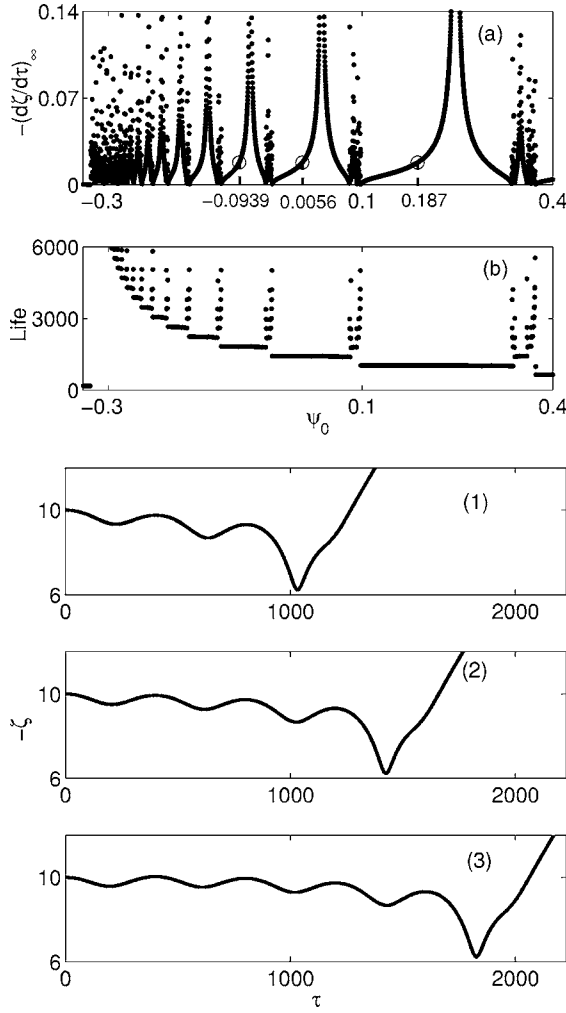The general solution of this equation is

FIG. 7. (a) The exit velocity versus initial phase difference graph of Fig. 6(a) replotted near the accumulation point of the primary hill sequence; (b) the lifetime versus initial phase difference graph; (1)–(3) separation ($-\zeta$) versus time (τ) diagrams at three values of ψ_0 marked by circles in (a): (1) 0.187; (2) 0.0056; and (3) -0.0939. All these graphs are obtained from the ODE model (4.42) and they should be compared to the corresponding PDE graphs in Fig. 2.

$$Y(\tau) = \ln[-2C_1^2 \operatorname{sech}^2(C_1\tau + C_2)], \qquad (5.3)$$

where

$$C_1 = \frac{1}{2}\sqrt{\dot{Y}_0^2 - 2e^{Y_0}} = \frac{1}{\sqrt{2}}\sqrt{E + iM} \qquad (5.4)$$

and

$$C_2 = -\operatorname{arctanh}\left(\frac{\dot{Y}_0}{2C_1}\right). \qquad (5.5)$$

Here the branch of the square root function in Eq. (5.4) is chosen such that $\operatorname{Re}(C_1) \geq 0$. It is noted that solutions Y which differ by a multiple of $2\pi i$ correspond to the same physical solution, thus it does not matter which Riemann surface one takes for the logarithmic function in Eq. (5.3). If

$C_1 = 0$, i.e., $\dot{Y}_0 = \pm\sqrt{2}e^{Y_0/2}$, the solution (5.3) degenerates to the form

$$Y(\tau) = -2\ln\left(e^{-1/2Y_0} \mp \frac{1}{\sqrt{2}}\tau\right). \qquad (5.6)$$

The asymptotic behaviors of these solutions as $\tau \to \infty$ can be easily determined. Let

$$C_1 = a + bi, \quad \frac{C_2}{C_1} = c + di, \qquad (5.7)$$

where a, b, c, and d are real constants, then the following leading-order asymptotic expressions for the solution can be obtained when $\tau \to \infty$:

(1) $a \neq 0$: $\quad Y(\tau) \to -2|a|\tau - \operatorname{sgn}(a)2b\tau i;$ $\qquad (5.8)$

(2) $a = 0$, $\quad b \neq 0$:

    (2a) $d = 0$:

$$Y(\tau) = \ln 2b^2 - \ln\cos^2 b(\tau + c); \qquad (5.9)$$

    (2b) $d \neq 0$:

$$Y(\tau) = \ln 4b^2 - \ln[\cosh 2bd + \cos 2b(\tau + c)]$$
$$+ 2i\arctan[\tanh(bd)\tan b(\tau + c)]; \qquad (5.10)$$

(3) $a = 0$, $\quad b = 0$: $\quad Y(\tau) \to -2\ln(\mp\tau).$ $\qquad (5.11)$

From these asymptotic expressions, we see that when $a \neq 0$, the two solitary waves eventually move away from each other with exit velocity $2|a|$; when $a = 0$ but $b \neq 0$, the solution is time-periodic for both $d = 0$ and $d \neq 0$, the difference being that in the former case, the periodic solution exhibits finite-time singularities [where $\zeta = \operatorname{Re}(Y) \to \infty$], while in the latter case, the solution has no singularities; when $a = b = 0$, the two solitary waves eventually separate logarithmically, and the exit velocity is zero. As an example, we take the initial conditions (4.44). In this case, the graph of exit velocity $-\dot{\zeta}_\infty (= 2|a|)$ versus ψ_0 is plotted in Fig. 9 (bottom panel). This graph is smooth everywhere, except at $\psi_0 = 0, \pm\pi$ where it has a cusp (due to the absolute-value function in $|a|$). The squares and diamonds on this graph will be explained later. Clearly, this graph has no fractal structure anywhere. Thus fractal dependence is a signature of the dynamical system (4.42) when it is nonintegrable (with $\varepsilon \neq 0$), not when it is integrable (with $\varepsilon = 0$).

The above asymptotic states do not tell the full story about the solution dynamics in the integrable system. For instance, for the case of $a \neq 0$, even though the solution has a benign-looking asymptotics (5.8) as $\tau \to \infty$, the solution can still develop a singularity (where the separation $\zeta \to \infty$) at a finite time. These solutions with finite-time singularities turn out to be critical for the appearance of fractal structures in the nonintegrable system, as our numerics in the next section will indicate. Thus we analyze these singularity solutions in more detail below. The necessary and sufficient conditions for singularities in solution (5.3) are that
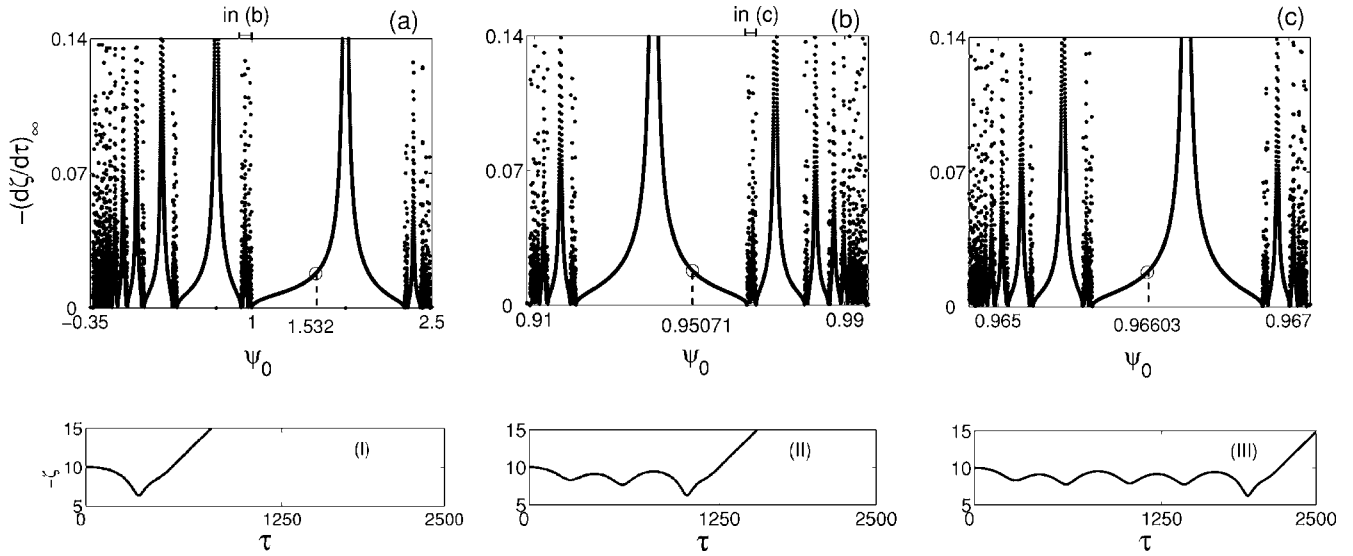
FIG. 8. Top: the exit velocity versus initial phase difference graph of Fig. 6(a) and its two zoomed-in structures. Bottom: separation versus time diagrams at three values of ψ_0 marked by circles in the top panel: (1) 1.532; (2) 0.950 71; and (3) 0.966 03. These graphs from the ODE model should be compared to the corresponding PDE graphs in Fig. 3.

$$\cosh(C_1 \tilde{\tau} + C_2) = 0, \tag{5.12}$$

and $\tilde{\tau} > 0$, where $\tilde{\tau}$ is the time of singularity. If $\tilde{\tau} < 0$, i.e., singularities in the solution occur at a negative time, such singularities are irrelevant for the time evolution of Eq. (4.42) and need not be considered. The solutions of Eq. (5.12) are

$$C_1 \tilde{\tau} + C_2 = \frac{1}{2}(2n + 1)\pi i, \quad n = 0, \pm 1, \pm 2, \dots . \tag{5.13}$$

This is a complex-valued relation, which gives two real relations on $\tilde{\tau}$, C_1, and C_2. When $a \neq 0$, i.e., C_1 is not purely imaginary, we find by separating the real and imaginary parts of Eq. (5.13) that the solution (5.3) has a single finite-time

TABLE I. Comparison of locations and lifetimes of primary hills in Figs. 2(a) and 7(a) from the PDE and ODE simulations.

n	Location (PDE) $\Delta\phi_{0,n}$	Location (ODE) $\psi_{0,n}$	Life (PDE) t_n	Life (ODE) $\sqrt{f}\tau_n$
1	1.7735	1.7794	65	68
2	0.6985	0.7015	117	119
3	0.2430	0.2468	183	185
4	0.0280	0.0359	253	255
5	−0.0850	−0.0763	325	327
6	−0.1530	−0.1431	398	400
7	−0.1963	−0.1863	470	473
8	−0.2258	−0.2157	544	547
9	−0.2475	−0.2367	617	620
10	−0.2630	−0.2523	691	693
∞	−0.3392	−0.3280	∞	∞

singularity of the type $\ln(\tau - \tilde{\tau})$ if the following conditions are satisfied:

$$S \equiv \frac{\mathrm{Im}(C_1^* C_2)}{\mathrm{Re}(C_1)} = \frac{1}{2}(2n + 1)\pi, \quad n = 0, \pm 1, \pm 2, \dots , \tag{5.14}$$
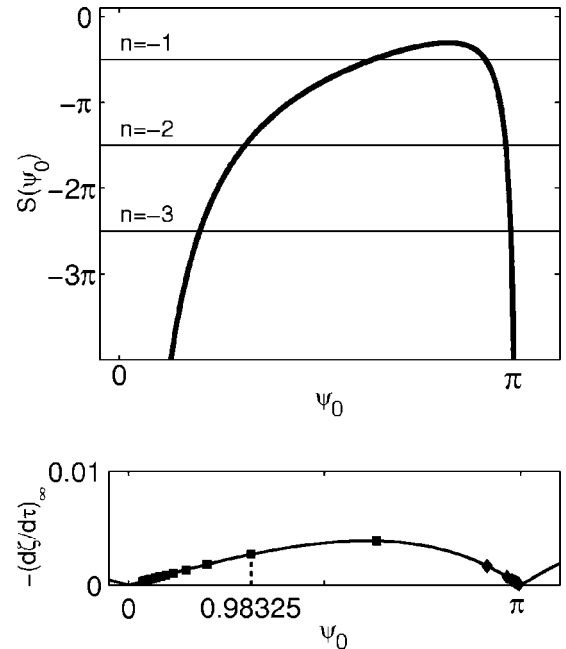

FIG. 9. Top: graph of the function $S(\psi_0)$ defined in Eq. (5.14) for the initial conditions (4.44). Intersections of the graph with horizontal lines are singularity points. Bottom: exit velocity versus ψ_0 graph in the integrable system (4.42). Both squares and diamonds are singularity points.

$$\widetilde{\tau} = -\frac{\text{Re}(C_2)}{\text{Re}(C_1)} > 0. \qquad (5.15)$$

Here $\text{Re}(\cdot)$ and $\text{Im}(\cdot)$ represent the real and imaginary parts of a complex number. When $a=0 (b \neq 0)$, singularity solutions exist if $d=0$. These solutions have an infinite number of finite-time singularities of the type $\ln(\tau - \widetilde{\tau})$, as the formula (5.9) indicates. Physically, at the time of singularity $\widetilde{\tau}$, the two solitary waves strongly collide, thus $\widetilde{\tau}$ is the collision time. Whether conditions (5.14) and (5.15) can be satisfied depends on the initial conditions [which determine the C_1 and C_2 values, see Eqs. (5.4) and (5.5)]. In the text below, we will call initial conditions $(\zeta_0, \dot{\zeta}_0, \psi_0, \dot{\psi}_0)$ which satisfy Eqs. (5.14) and (5.15) as singularity points. At singularity points, solutions of the integrable dynamical system (4.42) develop finite-time singularities.

To demonstrate how to determine singularity points in the initial-condition space, we take initial conditions (4.44) of Fig. 6(a) as an example. Here ψ_0 is a control parameter. With these initial conditions, the graph of function $S(\psi_0)$ is plotted in Fig. 9 (top panel). This graph has a maximum of 0.96. As $\psi_0 \to 0^+$ or π^-, $S(\psi_0) \to -\infty$. As we can see from this graph, for any value of $n \leq -1$, Eq. (5.14) has two roots, $\psi_{0,n}^{(1)}$ and $\psi_{0,n}^{(2)}$. We have checked that these roots satisfy the other singularity condition (5.15), thus these $\psi_{0,n}^{(1)}$ and $\psi_{0,n}^{(2)}$ values are singularity points. It is noted that the graph of function $S(\psi_0)$ also has another piece in the interval $\pi < \psi_0 < 2\pi$, which is the mirror image of that shown in Fig. 9 around the point $\psi_0 = \pi$; but in that interval, $\widetilde{\tau} < 0$, not satisfying the second singularity condition (5.15), thus we did not plot that piece of the graph in Fig. 9.

Next, we examine these singularity points $\psi_{0,n}^{(1)}$ and $\psi_{0,n}^{(2)}$ in more detail. These points form two infinite sequences with $n = -1, -2, \ldots$, which accumulate at $\psi_0 = 0^+$ and π^-, respectively. In Fig. 9 (bottom panel), these two sequences are marked by squares and diamonds on the exit velocity versus ψ_0 graph. Calculating the asymptotics of C_1 from Eq. (5.14) and substituting it into Eq. (5.15), we find that the collision times $\widetilde{\tau}_n$ of both sequences have the following asymptotic expressions:

$$\omega \widetilde{\tau}_n = 2|n|\pi + \pi, \quad n \to -\infty, \qquad (5.16)$$

where $\omega = 2 \, \text{Im}(C_1|_{\psi_0=0})$ and $2 \, \text{Im}(C_1|_{\psi_0=\pi})$ for the left and right sequences, respectively. The asymptotic formulas for the locations of these two singularity sequences $\{\psi_{0,n}^{(1)}\}$ and $\{\psi_{0,n}^{(2)}\}$ can also be calculated. We find from Eq. (5.14) that

$$\psi_{0,n}^{(1)} \to \frac{A_1}{(2n+1)\pi}, \quad n \to -\infty \qquad (5.17)$$

and

$$\pi - \psi_{0,n}^{(2)} \to \frac{A_2}{(2n+1)\pi}, \quad n \to -\infty, \qquad (5.18)$$

where

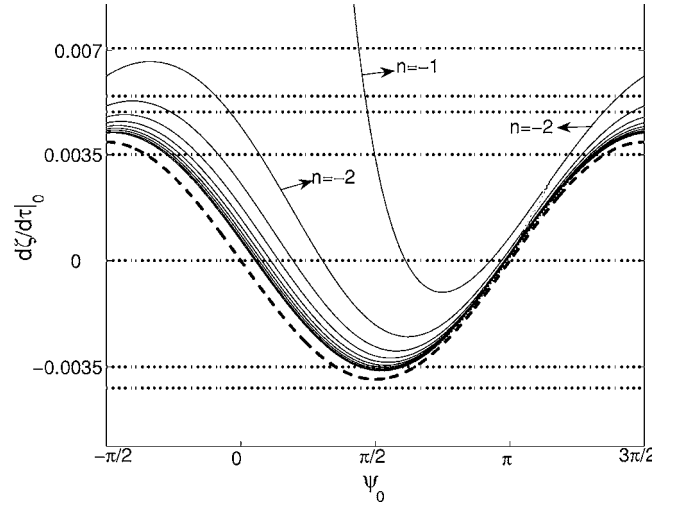$$A_1 = 8e^{-\zeta_0} \text{Re}(C_2) \text{Im}^2 (C_1)|_{\psi_0=0}$$

and

FIG. 10. Singularity points satisfying conditions (5.14) and (5.15) in the $(\psi_0, \dot{\zeta}_0)$ plane. The dashed curve is the accumulation curve. Here $\zeta_0 = -10$, $\dot{\psi}_0 = -0.011\,67$.

$$A_2 = 8e^{-\zeta_0} \text{Re}(C_2) \text{Im}^2 (C_1)|_{\psi_0=\pi}.$$

The above detailed analysis on singularity points was performed for the particular initial conditions (4.44) where the two solitary waves are initially stationary ($\dot{\zeta}_0 = 0$). What will happen if $\dot{\zeta}_0 \neq 0$? To answer this question, we fix ζ_0 and $\dot{\psi}_0$ as in Eq. (4.44), vary $\dot{\zeta}_0$, and examine how singularity points move in the $(\psi_0, \dot{\zeta}_0)$ plane. The results are shown in Fig. 10. The top curve corresponds to $n = -1$, the next curve corresponding to $n = -2$, and so on. All curves are bounded from both above and below except the top one (with $n = -1$). When $n \to -\infty$, these curves approach the accumulation curve plotted by the dashed line in Fig. 10. Below this accumulation curve, there are no singularity points. The analytical formula for this accumulation curve can be easily derived. On this accumulation curve, C_1 must be pure imaginary, thus

$$M = \dot{\zeta}_{0c} \dot{\psi}_0 - e^{\zeta_0} \sin \psi_0 = 0, \qquad (5.19)$$

$$E = \frac{1}{2}(\dot{\zeta}_{0c}^2 - \dot{\psi}_0^2) - e^{\zeta_0} \cos \psi_0 < 0. \qquad (5.20)$$

Here $(\dot{\zeta}_{0c}, \psi_0)$ is an accumulation point. From Eq. (5.19), we see that the function of the accumulation curve is

$$\dot{\zeta}_{0c} = \frac{e^{\zeta_0} \sin \psi_0}{\dot{\psi}_0}. \qquad (5.21)$$

The maximum and minimum of this curve are

$$\dot{\zeta}_{0c,\text{min}} = -\dot{\zeta}_{0c,\text{max}} = -\left|\frac{e^{\zeta_0}}{\dot{\psi}_0}\right|. \qquad (5.22)$$

For the ζ_0 and $\dot{\psi}_0$ values of Fig. 10, we get $\dot{\zeta}_{0c,\text{min}} = -0.003\,89$. If $\dot{\zeta}_0 < \dot{\zeta}_{0c,\text{min}}$, there are no singularity solutions for any value of ψ_0. When $\dot{\zeta}_{0c,\text{min}} < \dot{\zeta}_0 < \dot{\zeta}_{0c,\text{max}}$, two infinite

sequences of singularity points can be found. When $\dot{\zeta}_0 > \dot{\zeta}_{0c,\max}$, however, the number of singularity points becomes finite; this number gradually decreases (down to one) as $\dot{\zeta}_0$ increases.

The above calculations of singularity points and their accumulation curves were made for special choices of initial conditions $\zeta_0 = -10$ and $\dot{\psi}_0 = -0.011\,67$ (see Fig. 10). In view of the importance of singularity points for fractal structures which we will reveal in the next section, we would like to discuss singularity points and their accumulation curves further for *general* initial conditions below.

First, we examine the accumulation curve in the $(\psi_0, \dot{\zeta}_0)$ plane for general initial conditions ζ_0 and $\dot{\psi}_0$. In this general case, the accumulation curve (if it exists) is necessarily given by Eq. (5.21). But the curve (5.21) (or portions of it) may not satisfy condition (5.20), and thus may not actually be the accumulation curve. Below we determine what portions of the curve (5.21) are the accumulation curve. Before we do so, let us first point out that conditions (5.19) and (5.20) are not only necessary, but also sufficient conditions for the accumulation curve. In addition, the accumulation of singularity points toward the accumulation curve is always from the upper side, not lower side. To show these, we only need to prove that condition (5.15) holds only on the upper edge of the curve (5.21), but not the lower edge of it. On the upper edge of curve (5.21), C_1 is purely imaginary, and sgn(M) =sgn$(\dot{\psi}_0)$. Thus sgn(Im(C_1))=sgn(M)=sgn$(\dot{\psi}_0)$. Consequently, Re$(\dot{Y}_0/2C_1) > 0$. Notice that for any complex number z, Re[tanh(z)] and Re(z) have the same sign, hence Re$(C_2) < 0$. Then due to Re$(C_1) > 0$, condition (5.15) thus holds. By similar reasoning, we can show that on the lower edge of the curve (5.21), condition (5.15) does not hold. Thus singularity points accumulate toward curve (5.21) only from above, not below.

Now we turn to Eqs. (5.19) and (5.20), and use them to determine the accumulation curve for the general case. Substituting Eq. (5.21) into inequality (5.20) and simplifying, this inequality becomes

$$-\frac{1}{\dot{\psi}_0^2}(\dot{\psi}_0^2 + e^{\zeta_0}(1 + \cos\psi_0))(\dot{\psi}_0^2 - e^{\zeta_0}(1 - \cos\psi_0)) < 0,$$

$$(5.23)$$

which is equivalent to

$$\cos\psi_0 > 1 - e^{-\zeta_0}\dot{\psi}_0^2. \tag{5.24}$$

Thus the accumulation curve is the parts of curve (5.21) where ψ_0 satisfies the constraint (5.24). If $\dot{\psi}_0^2 > 2e^{\zeta_0}$, condition (5.24) is satisfied for all values of ψ_0, hence the entire curve (5.21) is the accumulation curve. If $0 < \dot{\psi}_0^2 \leq 2e^{\zeta_0}$, portions of the curve (5.21) centered at $\psi_0 = \pi$ do not satisfy condition (5.24), and thus do not belong to the accumulation curve. The rest of the curve (5.21) does satisfy condition (5.24), and thus is the accumulation curve. If $\dot{\psi}_0 = 0$ (equal initial ψ_0) satisfies condition (5.24), thus accumulation points do not exist.

Next, we derive two general properties about singularity points in the $(\psi_0, \dot{\zeta}_0)$ plane for general initial conditions ζ_0 and $\dot{\psi}_0$. One property is that, if $\dot{\zeta}_{0c}$ is on the accumulation curve, then for any $\dot{\zeta}_0 < \dot{\zeta}_{0c}$, singularity points cannot exist. We will prove this by showing that $\tilde{\tau} < 0$ for $\dot{\zeta}_0 < \dot{\zeta}_{0c}$. To show $\tilde{\tau} < 0$, we only need to show Re$(\dot{Y}_0/2C_1) < 0$ (see above). Without loss of generality, we only show this for $\dot{\psi}_0 < 0$; the proof for $\dot{\psi}_0 > 0$ is similar (in fact, as has been pointed out before, flipping the sign of $\dot{\psi}_0$ physically amounts to interchanging the positions of the left and right solitary waves and thus does not affect the interaction outcome). For $\dot{\psi}_0 < 0$ and $\dot{\zeta}_0 < \dot{\zeta}_{0c}$, C_1 is in the first quadrant (as $M > 0$). If $\dot{\zeta}_0 < 0$, then $\dot{Y}_0$ is in the third quadrant, thus Re$(\dot{Y}_0/2C_1) < 0$ holds. Now we consider $0 < \dot{\zeta}_0 < \dot{\zeta}_{0c}$. In this case, $\dot{Y}_0$ is in the fourth quadrant, hence $i\dot{Y}_0$ lies in the first quadrant (like C_1). To show Re$(\dot{Y}_0/2C_1) < 0$, we only need to show arg$(i\dot{Y}_0) < $ arg$(2C_1)$. Since both $i\dot{Y}_0$ and C_1 are in the first quadrant, we only need to show arg$(-\dot{Y}_0^2) < $ arg$(4C_1^2)$. Notice that

$$-\dot{Y}_0^2 + 4C_1^2 = -2e^{Y_0}, \tag{5.25}$$

which is independent of $\dot{\zeta}_0$. In addition, the angle of $-2e^{Y_0}$ falls in between those of $-\dot{Y}_0^2$ and $4C_1^2$. Thus to show arg$(-\dot{Y}_0^2) < $ arg$(4C_1^2)$, we only need to show arg$(-\dot{Y}_0^2) < $ arg$(-2e^{Y_0})$. Note that

$$-\dot{Y}_0^2 = \dot{\psi}_0^2 - \dot{\zeta}_0^2 - 2i\dot{\psi}_0\dot{\zeta}_0, \tag{5.26}$$

whose angle is an increasing function of $\dot{\zeta}_0$ when $\dot{\psi}_0 < 0$, thus for $\dot{\zeta}_0 < \dot{\zeta}_{0c}$,

$$\arg(-\dot{Y}_0^2) < \arg(\dot{\psi}_0^2 - \dot{\zeta}_{0c}^2 - 2i\dot{\psi}_0\dot{\zeta}_{0c}). \tag{5.27}$$

Now recall that $\dot{\zeta}_{0c}$ lies on the accumulation curve, thus it satisfies the conditions (5.19) and (5.20). Substituting these conditions into Eq. (5.27), and recalling our assumptions of $\dot{\psi}_0 < 0$ and $0 < \dot{\zeta}_0 < \dot{\zeta}_{0c}$, we find that the right-hand side of Eq. (5.27) is less than arg$(-2e^{Y_0})$, thus inequality arg$(-\dot{Y}_0^2) < $ arg$(-2e^{Y_0})$ is proved. Summarizing the above arguments, we conclude that for any $\dot{\zeta}_0$ below the accumulation curve, singularity points do not exist in the $(\psi_0, \dot{\zeta}_0)$ plane.

Another general property about singularity points is that, at sufficiently large values of $\dot{\zeta}_0$, there is a unique singularity point in the ψ_0 interval. The proof is as follows. It is easy to check that when $\dot{\zeta}_0^2 + \dot{\psi}_0^2 \gg e^{\zeta_0}$ and $|\dot{\zeta}_0| \gtrsim |\dot{\psi}_0|$, functions S and $\tilde{\tau}$ have the following leading-order asymptotic expressions:

$$\tilde{\tau} \rightarrow \frac{1}{\dot{\zeta}_0}\ln\frac{2(\dot{\zeta}_0^2 + \dot{\psi}_0^2)}{e^{\zeta_0}}, \tag{5.28}$$

$$S \to \frac{1}{2}\,\text{sgn}(\dot{\zeta}_0)\psi_0 + S_A, \qquad (5.29)$$

where

$$S_A = \frac{\dot{\psi}_0}{2|\dot{\zeta}_0|}\ln\frac{2(\dot{\zeta}_0^2 + \dot{\psi}_0^2)}{e^{\zeta_0}} - \arctan\frac{\dot{\psi}_0}{|\dot{\zeta}_0|} - \frac{1}{2}\pi, \quad (5.30)$$

and the relative errors are $O(e^{\zeta_0}/(\dot{\zeta}_0^2 + \dot{\psi}_0^2))$. From Eq. (5.29), we see that the rise of the S value over the interval $0 \le \psi_0 \le 2\pi$ is π, which guarantees that Eq. (5.14) has a single solution in the ψ_0 interval for a single value of n. From Eq. (5.28), we see that when $\dot{\zeta}_0 > 0$ is sufficiently large, $\tilde{\tau} > 0$ over the entire ψ_0 interval. Thus singularity conditions (5.14) and (5.15) admit a unique singularity point. We note in passing that when $\dot{\zeta}_0$ is sufficiently large negative, $\tilde{\tau} < 0$ over the entire ψ_0 interval, thus there cannot be any singularity points. This is consistent with the previous general property proved above.

To summarize the above results on singularity points and accumulation points and slightly extend them, we present the following classifications on singularity solutions in the integrable system (4.42).

(1) $\dot{\psi}_0 = 0$ (equal initial amplitudes).

    (a) If $\dot{\zeta}_0 > -\sqrt{2}e^{\zeta_0/2}$, a singularity solution exists at the single singularity point $\psi_0 = 0$. Here $M = 0$, and $E > 0$ for $\dot{\zeta}_0 > \sqrt{2}e^{\zeta_0/2}$ and $E < 0$ otherwise.

    (b) If $\dot{\zeta}_0 < -\sqrt{2}e^{\zeta_0/2}$, there are no singularity solutions for any ψ_0.

(2) $\dot{\psi}_0 \neq 0$, $\dot{\zeta}_0 = 0$ (nonequal initial amplitudes, zero initial velocities).

    (a) If $\dot{\psi}_0^2 > 2e^{\zeta_0}$, singularity solutions exist at two infinite sequences of ψ_0 values, accumulating at $\psi_0 = \{0^+, \pi^-\}$, or $\{\pi^+, 2\pi^-\}$, for $\dot{\psi}_0 < 0$ and $\dot{\psi}_0 > 0$, respectively.

    (b) If $0 < \dot{\psi}_0^2 < 2e^{\zeta_0}$, singularity solutions exist at one infinite sequence of ψ_0 values, accumulating at $\psi_0 = 0^+$ or $2\pi^-$ for $\dot{\psi}_0 < 0$ and $\dot{\psi}_0 > 0$, respectively.

On these sequences of singularity points, $M \neq 0$ and $E \neq 0$ generically (at the accumulation points, $M = 0$, and $E < 0$).

(3) $\dot{\psi}_0 \neq 0$ (the general nonequal initial amplitude case).

In this case, the accumulation curve is the parts of curve (5.21) where ψ_0 satisfies the constraint (5.24). When $\dot{\psi}_0^2 > 2e^{\zeta_0}$, the entire curve (5.21) is the accumulation curve. When $0 < \dot{\psi}_0^2 \le 2e^{\zeta_0}$, the accumulation curve is curve (5.21) except portions of it which are centered at $\psi_0 = \pi$. For $\dot{\zeta}_0$ below the accumulation curve, there are no singularity points; at sufficiently large $\dot{\zeta}_0$ values, there is a single singularity point. At all these singularity values, E and M are nonzero generically (except the accumulation points where $M = 0$).
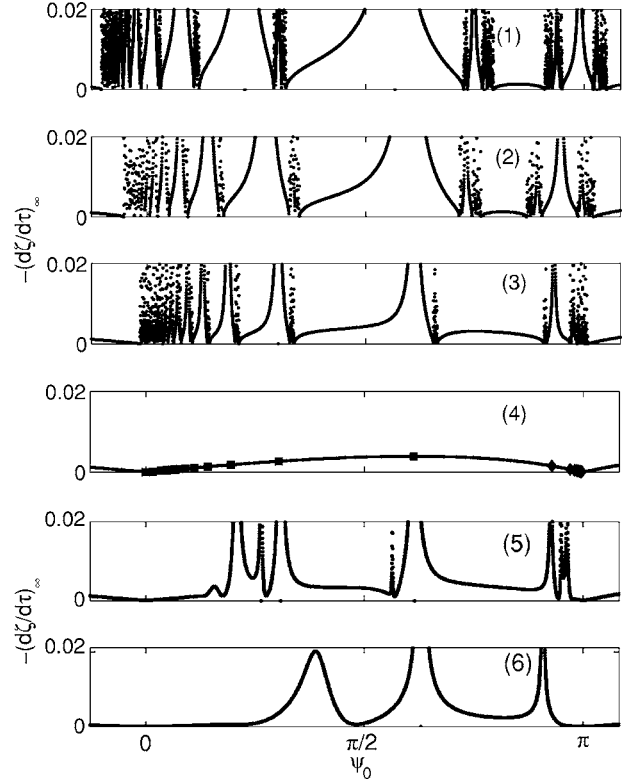

FIG. 11. The exit velocity versus initial phase difference graphs in the ODE model (4.42) at various values of ε: (1) 0.136 65; (2) 0.036; (3) 0.0036; (4) 0; (5) −0.0036; and (6) −0.036. The initial conditions are given in Eq. (4.44). The squares and diamonds in (4) are singularity points of the integrable system (see Fig. 9, bottom).

It is noted that in the above classifications, case (2) is just a special case of case (3), and can be readily deduced from case (3). Case (1) can be deduced from case (3) as well under the limit $\dot{\psi}_0 \to 0$. But cases (1) and (2) are important special cases, hence we listed them out separately.

VI. ORIGINS OF FRACTAL STRUCTURES IN THE NONINTEGRABLE DYNAMICAL EQUATIONS

We have known from Figs. 6–8 that the nonintegrable ODE system (4.42) exhibits hill sequences and fractal structures which coincide with those in the PDE simulations, but such structures do not exist when this ODE system becomes integrable. The natural question then is, where do the fractal structures in the nonintegrable system (4.42) come from? In this section, we will establish through careful numerics that these fractal structures bifurcate from singularity points of the integrable system.

To determine the origin of these fractals, we take the same initial conditions (4.44) as in Fig. 6(a), but gradually decrease the value of ε from 0.136 65 of Fig. 6(a) down to zero (the integrable case), then down further to negative values. In this process, we closely monitor how the fractal structure of Fig. 6(a) changes as ε decreases. The result is shown in Fig. 11. Here, the $-\dot{\zeta}_\infty$ versus ψ_0 graphs are plotted at six decreasing ε values: $\varepsilon = 0.136\,65$, 0.036, 0.0036, 0, −0.0036, and

−0.036. We see that as ε decreases from 0.136 65 but above zero, primary hill sequences and the fractal regions between them persist and are clearly visible in Figs. 11(1–3). Indeed, we have zoomed into the sensitive regions between primary hills in each of Figs. 11(1–3), and obtained higher order structures which look very similar to those shown in Fig. 8. As $\varepsilon \rightarrow 0^+$, our key observation is that the peaks of individual primary hills as well as the nearby fractal regions collapse to sequences of points on the smooth $-\dot{\zeta}_\infty$ curve of the integrable system [see Figs. 11(3 and 4)]. Closer examination tells us that these sequences of points in Fig. 11(4) are nothing but the two sequences of singularity points of the integrable system which we plotted in Fig. 9. In other words, hill sequences and fractal structures in the nonintegrable system bifurcate from the singularity points of the integrable system. However, this bifurcation is one-sided: as ε decreases below zero, no fractal regions appear, see Fig. 11(5). A finite number of primary hills, reminiscent of primary hill sequences for positive ε values, do exist; but the whole graph is smooth, and it has no fractal structures inside [even the spike-looking parts of the graph in Fig. 11(5) turn out to be smooth upon closer examination. Furthermore, as ε decreases further below zero, the number of primary hills keeps decreasing, and the graph becomes more smooth, see Fig. 11(6). Thus fractal structures are a signature of the nonintegrable system (4.42) only for positive values of ε, not negative values of ε.

To further substantiate our claim on fractal structures of the nonintegrable system bifurcating from singularity points of the integrable system, we tune initial conditions so that singularity points in the integrable system gradually disappear in the ψ_0 interval, and check if fractal structures in the nonintegrable system disappear as well (for small ε). Specifically, we fix the ζ_0 and $\dot{\psi}_0$ values in Eq. (4.44) and tune the $\dot{\zeta}_0$ value, as we did in Fig. 10. The ε value in Eq. (4.42) is taken as $\varepsilon=0.0036$, which is very small. Thus the nonintegrable system is weakly perturbed from the integrable one. For the above initial conditions, singularity points of the integrable system have been displayed in Fig. 10 in the $(\psi_0, \dot{\zeta}_0)$ plane. We gradually decrease the $\dot{\zeta}_0$ value. For each $\dot{\zeta}_0$, we numerically compute the exit velocity versus ψ_0 graph in the perturbed (nonintegrable) system (4.42), and compare how this graph relates to singularity points of the integrable system in Fig. 10. To illustrate, we pick seven representative $\dot{\zeta}_0$ values, which are 0.007 07, 0.005 48, 0.004 95, 0.003 50, 0, −0.003 50, and −0.004 24 in decreasing order. These seven $\dot{\zeta}_0$ values are marked by horizontal dashed lines in Fig. 10. As we can see from that figure, at these seven $\dot{\zeta}_0$ values, the numbers of singularity points in the ψ_0 interval are 1, 3, 5, ∞, ∞, ∞, and 0, respectively. For each of these seven $\dot{\zeta}_0$ values, the corresponding exit velocity versus ψ_0 graph in the perturbed system (4.42) is shown in Fig. 12. We notice from this figure that the numbers of primary hills and fractal regions near these hills at these $\dot{\zeta}_0$ values are equal to 1, 3, 5, ∞, ∞, ∞, and 0, respectively—exactly like singularity points in the integrable system. In particular, when singularity points in the integrable system disappear, so do primary hills and frac-
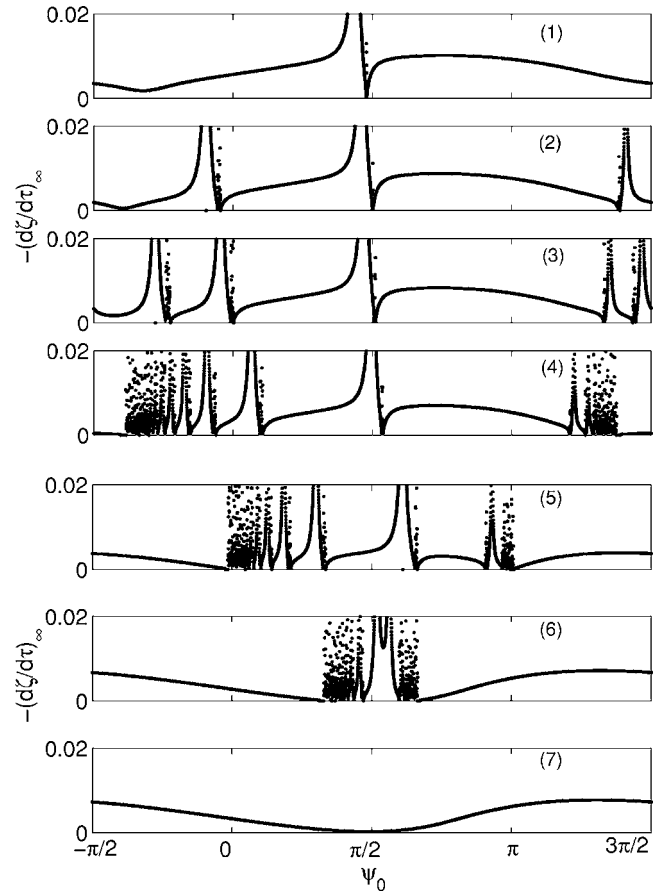

FIG. 12. The exit velocity versus initial phase difference graphs in the ODE model (4.42) at various values of $\dot{\zeta}_0$: (1) 0.007 07; (2) 0.005 48; (3) 0.004 95; (4) 0.003 50; (5) 0; (6) −0.003 50; and (7) −0.004 24. Here $\zeta_0=-10$, $\dot{\psi}_0=-0.011\,67$, and $\varepsilon=0.0036$.

tal structures in the weakly perturbed nonintegrable system. Furthermore, the locations of primary hills and fractal regions closely follow those of singularity points of the integrable system. Thus the connections between them are unmistakable. Figure 12, together with Fig. 11, establishes beyond doubt that primary hills and fractal structures in the nonintegrable system (4.42) indeed bifurcate from singularity points of the integrable system.

The bifurcation of fractal structures from singularity points of the integrable system indicates that near such points, the solutions of the perturbed system (4.42) are very sensitive to initial conditions. To shed light on why this sensitivity occurs, we present some numerical results below. First, we look at the integrable system (with $\varepsilon=0$). Taking the initial conditions as Eq. (4.44), evolutions of ψ versus τ at the singularity point $\psi_0=0.983\,25$ (marked in Fig. 9, bottom panel) and its left and right near neighbors $\psi_0=0.92$ and 1.05 are plotted in Fig. 13(a) using the solution formula (5.3). An interesting feature about these evolutions is that for initial ψ_0 values at the two sides of the singularity point, the phase functions $\psi(\tau)$ have drastically different trajectories as they go through the time $\tau \approx 700$ where the two solitary waves interact strongly (this time is the singularity time of the singular solution at $\psi_0=0.983\,25$). For ψ_0 below the sin-
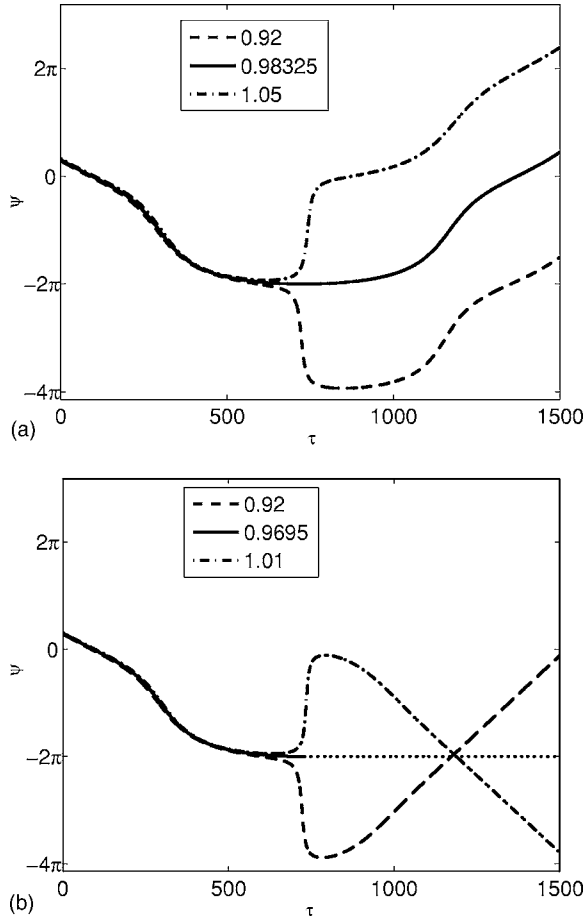
FIG. 13. Evolutions of ψ versus τ at a singularity point ψ_0 and its left and right neighbor points in the dynamical system (4.42) with initial condition (4.44). (a) $\varepsilon=0$ (the integrable case); here $\psi_0=0.983\,25$ is the singularity point which is marked in Fig. 9 (bottom panel); the left and right neighbor points are taken as $\psi_0=0.92$ and 1.05. (b) $\varepsilon=0.0036$ (the positively perturbed case); here $\psi_0=0.9695$ is the singularity point; its left and right neighbor points are taken as $\psi_0=0.92$ and 1.01.

gularity point, the phase sharply (but continuously) decreases by 2π, while for ψ_0 above the singularity point, the phase sharply (but continuously) increases by 2π. Recall that $\dot\psi \propto \Delta\beta$ and it determines the relative energy (amplitude) distributions among the two solitary waves [see Eqs. (4.37), (4.40), and (4.41)], we know that on the two sides of the singularity point, the energies have opposite distributions among the two solitary waves during their strong interactions. However, after the interaction is completed, the asymptotic slopes of the three $\psi(\tau)$ trajectories in Fig. 13(a) are almost the same, signaling that the interaction outcome is actually insensitive to the ψ_0 values (the roughly 2π difference between these phase trajectories does not affect the physical solutions). This is why outcomes of weak interactions in the integrable system (4.42) do not exhibit sensitive dependence on initial conditions (see Fig. 9, bottom panel). However, when system (4.42) is positively perturbed, the results are completely different. To demonstrate, we take $\varepsilon =0.0036$ now, while the initial conditions (4.44) remain the same. In this slightly perturbed system, the solution develops

finite-time singularity at the singularity point $\psi_0=0.9695$, which is the counterpart of the singularity point mentioned above in the integrable system. The phase function at this singularity point is plotted in Fig. 13(b) (solid line). [It is noted that in this perturbed case, we do not have exact solution formulas, hence this solution was obtained by numerically integrating Eq. (4.42). Due to the finite-time singularity in the solution, our numerical integration cannot go beyond the singularity time $\tau\approx700$. The solution beyond the singularity time, shown in Fig. 13(b) as dotted lines, was inferred from our numerics at nearby ψ_0 values.] On the two sides of the singularity point, we select two nearby values $\psi_0=0.92$ and 1.01. The phase trajectories at these ϕ_0 values are also plotted in Fig. 13(b). We see that as these trajectories go through the time $\tau\approx700$, one sharply decreases by 2π, while the other sharply increases by 2π, similar to what happens in the integrable case [see Fig. 13(a)]. However, after these sharp decreases/increases, the trajectories turn around and start to move in the opposite direction. Eventually, these trajectories approach drastically different asymptotic slopes (one positive and the other one negative in fact), indicating that the interaction outcomes are very different for these slight changes in the ψ_0 values. This is the phenomenon of sensitive dependence on initial conditions which occurs in the perturbed system (4.42) (with $\varepsilon>0$), but not the integrable system (with $\varepsilon=0$).

It is also enlightening to look at this sensitive dependence on initial conditions from the viewpoint of PDE evolutions. To illustrate, we take the cubic-quintic nonlinearity (2.7) in Eq. (2.1), and take $\alpha=1$, $\beta_0=1$. Then for the ε values and initial conditions used in the ODE simulations of Fig. 13, and in view of the variable rescalings (4.40) and (4.41), the corresponding PDE parameters for Fig. 13(a) (the integrable case) are $\gamma=0$, $\Delta\beta_0=-0.066\,016$, $\Delta V_0=0$, and $\Delta x_0=10$, and the corresponding PDE parameters for Fig. 13(b) (the perturbed case) are $\gamma=0.0010$, $\Delta\beta_0=-0.066$, $\Delta V_0=0$, and $\Delta x_0 =10$. For these PDE parameters, the PDE evolution results (in the form of contour plots) at three $\Delta\phi_0$ values corresponding to those in the ODE simulations of Fig. 13 are displayed in Fig. 14. In the integrable (NLS) case (top row of Fig. 14), we take the three $\Delta\phi_0$ values exactly the same as those in Fig. 13(a), i.e., $\Delta\phi_0=0.92\ 0.983\,25$, and 1.05. In this case, at the lower $\Delta\phi_0$ value, the left solitary wave retains its higher energy at the collision time; at the singularity point of $\Delta\phi_0$, the two waves completely coalesce at the collision time, signaling the singularity formation in the ODE system; at the higher $\Delta\phi_0$ value, the right solitary wave gets higher energy at the collision time. However, after interaction, the two waves always separate, and the right wave always gets higher energy, in all three cases. Recall that before interaction, the left wave has higher energy, thus we can call these interaction outcomes transmission. In these interactions, even though the intermediate process (especially the collision segment) rather strongly depends on the initial phase difference $\Delta\phi_0$, the interaction outcome is insensitive to it. These PDE evolution results completely resemble the ODE simulations in Fig. 13(a). In the perturbed (nonintegrable) case, the PDE simulation results are quite different from the integrable ones (as in the ODE simulations). In the perturbed case, we take the three $\Delta\phi_0$ values to be 0.92, 0.972, and
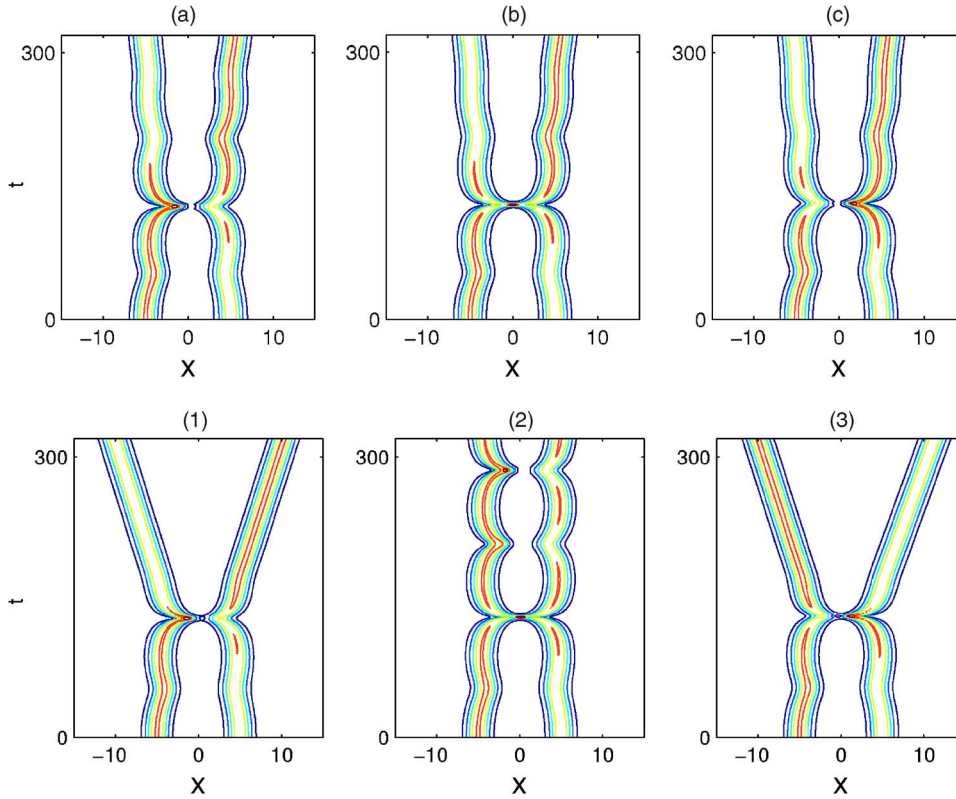
FIG. 14. (Color online) Evolutions of $|U(x,t)|$ in the PDE (2.1) with cubic-quintic nonlinearity (2.7), corresponding to the ODE simulations of Fig. 13. Top row: the integrable (NLS) equation ($\gamma = 0$); (a) $\Delta\phi_0 = 0.92$, (b) $\Delta\phi_0 = 0.983\,25$, and (c) $\Delta\phi_0 = 1.05$. Bottom row: the perturbed case (with $\gamma = 0.0010$); (1) $\Delta\phi_0 = 0.92$; (2) $\Delta\phi_0 = 0.972$; and (3) $\Delta\phi_0 = 1.01$. The values of other initial parameters are given in the text.

1.01. Notice that the first and third of these $\Delta\phi_0$ values are exactly the same as those in the ODE simulations of Fig. 13(b), while the middle $\Delta\phi_0$ value of 0.972 is slightly different from the corresponding ODE value of 0.9695. This slight difference in the middle $\Delta\phi_0$ value is necessary in order for the corresponding ODE and PDE simulations to exhibit the same behaviors, and this difference is due to the modeling error of the PDE evolutions by the ODE system (4.42). At $\Delta\phi_0 = 0.92$ [see Fig. 13(1)], the interaction outcome is similar to the integrable ones (top row of Fig. 13) in that it is also transmission; but at $\Delta\phi_0 = 0.972$ [Fig. 13(2)], the two waves strongly coalesce, then form an oscillating bound state. At $\Delta\phi_0 = 1.01$, on the other hand, the two exiting waves have opposite energy distributions from Fig. 13(1); this interaction outcome can be called reflection. Thus, in the perturbed case, the interaction outcome is sensitive to initial conditions, which distinctively contrasts the integrable case. Again, these PDE evolution results for the perturbed case completely resemble the ODE simulations in Fig. 13(b).

The above ODE and PDE simulations corroborate the fact that the source of this sensitive dependence on initial conditions in the perturbed system lies in the finite-time singularities of solutions in the integrable dynamical system (4.42). From the PDE point of view, the origin of this sensitive dependence can be traced to the coalescing of the two solitary waves in the integrable PDE system. At the moment, our understanding on this sensitive dependence and fractal structures in the perturbed system is still very limited. For instance, we cannot yet explain any quantitative details inside these fractal structures, nor can we explain why this sensitive

dependence occurs only for one-sided perturbations of the integrable system (with $\varepsilon > 0$). These are nontrivial questions which merit further analysis, but they are beyond the scope of the present paper.

The fact of primary hills and fractal structures in the nonintegrable system (4.42) bifurcating from singularity points of the integrable system has far reaching consequences. One important consequence is that the main features of primary hill sequences shown in Figs. 2(a) and 7(a) for PDEs and ODEs can now be analytically explained. For instance, the lifetime formula (3.6) for primary hill sequences in the weakly perturbed system (4.42) is nothing but the analogous collision-time (singularity time) formula (5.16) for sequences of singularity points in the integrable system. To make a quantitative comparison between these formulas, we take the initial condition (4.44) which was used in the PDE and ODE simulations of Figs. 2(a) and 7(a). When the time rescaling (4.41) is recovered, the collision-time formula (5.16) of the integrable system becomes

$$0.0839\tilde{t}_n = 2n\pi + \pi, \qquad (6.1)$$

which compares very favorably with the lifetime formulas (3.6), (3.7), and (4.46) in direct PDE and ODE simulations. The small differences in the ω and δ values between the analytical formula (5.16) and the PDE/ODE ones (3.6) are caused by the not-so-small value of $\varepsilon = 0.136\,65$. As $\varepsilon \to 0$, these quantitative differences will vanish. Regarding the locations of individual hills in the primary-hill sequence, they

are described by the formula (5.17) for singularity-point locations of the integrable system when $\varepsilon \ll 1$. Note that the form of this formula is different from all previous ones on window sequences in solitary-wave collisions [15,16,20,25,29].

For $\varepsilon > 0$, each primary hill is paired with a sensitive (fractal) region at its foot (see Figs. 11 and 12). Similar to primary hill sequences, the locations of these fractal regions are described by the same formula (5.17) in the limit $\varepsilon \rightarrow 0^+$.

The fact of primary hills and fractal structures bifurcating from singularity points of the integrable system also explains major features of interaction results in Fig. 5(a) for the exponential nonlinearity (3.8). We have noticed that, unlike Fig. 1, this graph has only one infinite sequence of primary hills accumulating toward the left (the right sequence of Fig. 1 is absent). This phenomenon is due to the fact that for the choices of initial conditions for Fig. 5(a), there is only one infinite sequence of singularity points in the integrable system. To see it, we first calculate the f, g, and ε values for Fig. 5(a), which are found to be

$$f = 228.8211, \quad g = 231.917\,70, \quad \varepsilon = 0.013\,53. \quad (6.2)$$

Thus in the scaled dynamical equation (4.42), the initial conditions corresponding to those for Fig. 5(a) are

$$\zeta_0 = -12.132\,60, \quad \dot{\zeta}_0 = 0, \quad \dot{\psi}_0 = -0.002\,97. \quad (6.3)$$

Notice that $\dot{\psi}_0^2 < 2e^{\zeta_0}$, thus according to the classifications of singularity points in the end of the previous section (case 2), the integrable equation (4.42) with the above initial conditions has only one sequence of singularity points in the ψ_0 interval, accumulating to the left toward $\psi_0 = 0^+$. This is in perfect agreement with the primary-hill sequence of Fig. 5(a) from direct PDE simulations.

In many of the interaction results presented in this paper, the exit velocity versus ψ_0 graphs have infinite sequences of primary hills (see Figs. 1 and 5, for instance); when zooming into the sensitive regions between primary hills, one gets infinite sequences of secondary hills. It is important to understand that these two infinite sequences are pure coincidence, and are totally unrelated. Each primary hill corresponds to a particular singularity point of the integrable system, thus the number of primary hills is equal to the number of singularity points in the integrable system. This number can be either infinite or finite, depending on the choices of initial conditions. For instance, Figs. 12(1–3) have 1, 3, and 5 primary hills, corresponding to the same numbers of singularity points on the top three dashed lines of Fig. 10. On the other hand, at the foot of each primary hill, there is always an *infinite* sequence of secondary hills (when $\varepsilon > 0$). In other words, secondary hills always exist as an infinite, not finite, sequence. For example, if one zooms into each of the three sensitive regions at the foot of the three primary hills in Fig. 12(2), one always gets an infinite sequence of secondary hills. Thus secondary-hill structures are unrelated to primary-hill structures. If we zoom into the sensitive regions between secondary hills, we always get infinite sequences of tertiary hills which are very similar to the sequences of secondary

hills both qualitatively and quantitatively [see Figs. 3(b) and 3(c)]. This process can continue indefinitely. Thus our conclusion is that sensitive regions between primary hills are fractal structures (in the sense that portions of these structures, when amplified, are the same as the structures themselves); but the whole graph with primary hills is not a fractal.

VII. APPLICATIONS TO THE GENERALIZED NLS EQUATIONS WITH VARIOUS NONLINEARITIES

In previous sections, we have shown that for the cubic-quintic and exponential nonlinearities at selected parameters ($\alpha = 1$, $\gamma = 0.04$, $\beta_0 = 1$ for the former, and $\beta_0 = 2.3$ for the latter), weak interactions of solitary waves exhibit hill sequences and fractal structures for a wide range of initial conditions, and the reduced ODE model (4.42) accurately captures these interaction dynamics both qualitatively and quantitatively. In this section, we consider a larger question: for a given form of nonlinearity in the PDE (2.1), can it exhibit fractal structures? For example, with the cubic-quintic nonlinearity (2.7), for what parameters α and γ can one possibly find fractal structures? This question can be answered by applying our previous results on the ODE model (4.42). For demonstration purposes, we will do so for three forms of nonlinearity: cubic-quintic, exponential, and saturable nonlinearities.

From the analysis of the ODE system (4.42) in the previous section, we have found that fractal structures in weak interactions can only occur for $\varepsilon > 0$, not for $\varepsilon < 0$. Thus once we have obtained the functional dependence of ε on system parameters, it will quickly become clear when fractal structures can arise. The analytical expression for ε is given in Eq. (4.41). Notice that due to the Vakhitov-Kolokolov stability criterion [6,33], the solitary wave is linearly stable only when $P_\beta > 0$, i.e., $\varepsilon > -1$. Below, we will use the ε formula in Eq. (4.41) to calculate ε for general system parameters in the three nonlinearities mentioned above.

First we consider the cubic-quintic nonlinearity (2.7). When $\alpha < 0$, we found that P_β is always negative, i.e., the solitary wave is always linearly unstable. Thus we only consider the $\alpha > 0$ case below. In this case, it is easy to see from Eqs. (2.3) and (2.7) that by a rescaling of variables, we can make $\alpha = \beta_0 = 1$. Thus the only remaining parameter for this nonlinearity is γ. Using the analytical formula (2.9) for P, we can obtain the dependence of ε on γ, which is plotted in Fig. 15(1). From this graph, we see that $\varepsilon > 0$ when $\gamma > 0$, and $\varepsilon < 0$ when $\gamma < 0$. Thus *fractal structures in this cubic-quintic model can appear only when $\gamma > 0$, not when $\gamma < 0$.* If $\gamma = 0$, this cubic-quintic model reduces to the integrable NLS equation, and the dynamical equations (4.42) reduce to the integrable case (with $\varepsilon = 0$) studied in Sec. V. In this integrable case, there is of course no fractal dependence in solitary wave interactions.

Next, we consider the exponential nonlinearity (3.8). In this case, the solitary wave depends only on the propagation constant β, thus ε depends only on β as well. The analytical expression for function $\varepsilon(\beta)$ is not available, but this function can be easily determined by numerical methods, and its

graph is plotted in Fig. 15(b). It is seen that this graph has two critical propagation constants, $\bar{\beta}_a = 2.2457$ where $\varepsilon = 0$, and $\bar{\beta}_b = 14.0051$ where $\varepsilon = +\infty$. When $\beta < \bar{\beta}_a$, $\varepsilon < 0$, thus fractal structures do not exist; when $\bar{\beta}_a < \beta < \bar{\beta}_b$, thus fractal structures can appear (see previous sections); when $\beta > \bar{\beta}_b$, $\varepsilon < -1$, thus the solitary wave is linearly unstable.

Next, we consider the saturable nonlinearity,

$$F(|U|^2) = 1 - \frac{1}{1 + |U|^2}, \tag{7.1}$$

which is common in optics (for instance, in photorefractive crystals [38]). Here one is added in the above formula to make $F(0) = 0$ (this does not affect the solitary waves and their interaction dynamics). In this case, ε also depends only on the propagation constant β. This dependence is computed numerically and plotted in Fig. 15(c). We find that ε is negative for all values of β, thus fractal structures cannot exist in weak interactions of solitary waves for this saturable nonlinearity. This conclusion is consistent with our earlier results for the cubic-quintic nonlinearity, as the saturable nonlinearity (7.1) resembles the cubic-quintic nonlinearity (2.7) with $\alpha > 0$ and $\gamma < 0$. It is noted, however, that for the saturable nonlinearity, weak interactions of solitary waves can still exhibit some interesting structures as shown in Figs. 11(5, 6), but these structures are not fractal structures.

From the above three examples (as well as the previous section), we see that the reduced ODE model (4.42) enables us to accurately predict when and where fractal structures and hill sequences appear in the space of initial parameters of solitary waves. Based on this reduced model, a global and universal understanding on weak interactions of solitary waves has been achieved for the generalized NLS equations (2.1) with arbitrary forms of nonlinearity.

VIII. CONCLUSION AND DISCUSSION

In this paper, we have analyzed weak interactions of solitary waves in the generalized nonlinear Schrödinger equations with general forms of nonlinearity. We have shown that these interactions exhibit similar fractal dependence on initial conditions for different nonlinearities. To analytically explain these universal fractal structures, we derived a set of fourth-order dynamical equations for the solitary-wave parameters using asymptotic methods. A remarkable feature of these dynamical equations is that they contain only one parameter, which is dependent on the specific form of nonlinearity. When this parameter is zero, these dynamical equations are integrable, and the exact analytical solutions are derived. When this parameter is nonzero, the dynamical equations exhibit fractal structures which match those in the original PDEs both qualitatively and quantitatively. We have also investigated the origin of these fractal structures and found that they bifurcate from the singularity points (i.e., initial conditions for singularity solutions) in the integrable system. Based on this observation, an analytical criterion for the existence and locations of fractal structures is obtained. Lastly, we applied these analytical results to the generalized nonlinear Schrödinger equations with various nonlinearities
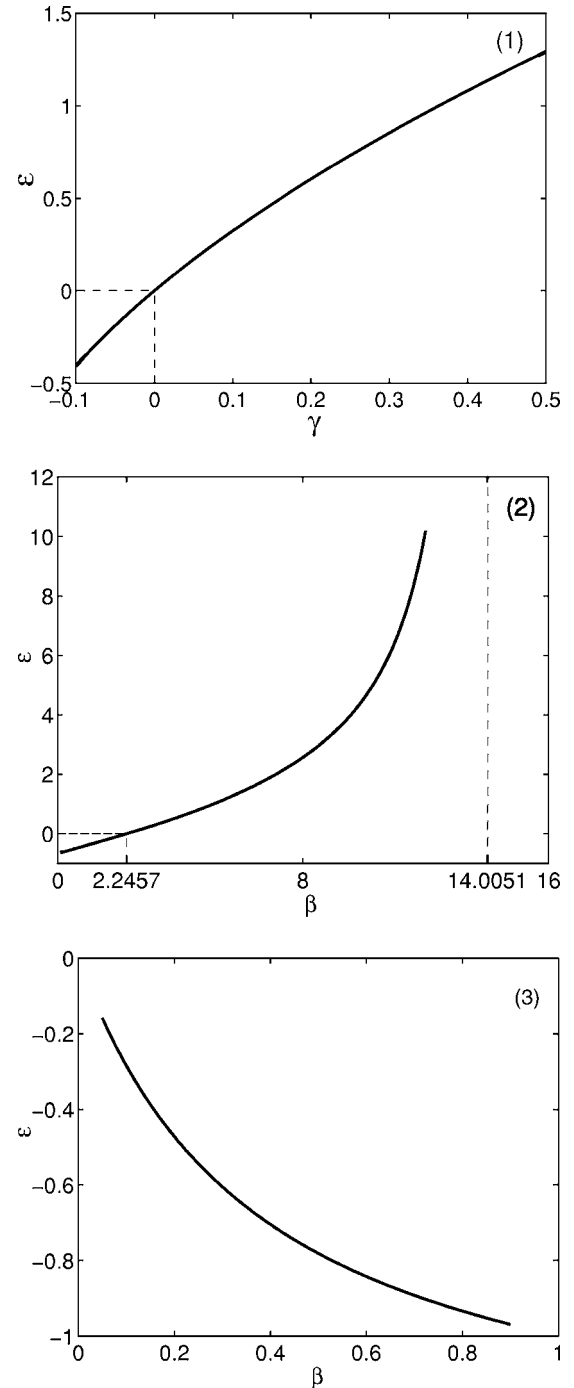

FIG. 15. Graphs of ε versus system parameters for three different nonlinearities: (1) ε versus γ for the cubic-quintic nonlinearity (2.7); (2) ε versus β for the exponential nonlinearity (3.8); and (3) ε versus β for the saturable nonlinearity (7.1).

such as the cubic-quintic, exponential and saturable nonlinearities, and predictions on their weak interactions of solitary waves are presented.

Regarding the bifurcation of fractal structures from the integrable dynamical equations, even though we have established that this bifurcation occurs at the singularity points of the integrable system, more challenging questions are to comprehensively analyze how this bifurcation takes place,

and to quantitatively predict the detailed geometric structures inside these fractals. This has not been done yet. Recently, Goodman and Haberman analyzed the approximate ODE models for the collisions of solitary waves in three physical systems where window sequences and fractal structures have been reported [28–30]. They found that the origin of window sequences and fractal structures in these systems lies in the crossing of the separatrix (homoclinic orbit). Analytical predictions on the locations of window sequences in the ODE models were derived as well. It is not clear at the moment whether similar analysis can be performed for our system (4.42). This question is beyond the scope of the present paper, and will be left for future studies.

[1] M. J. Ablowitz and H. Segur, *Solitons and the Inverse Scattering Transform* (SIAM, Philadelphia, 1981).

[2] A. Hasegawa and Y. Kodama, *Solitons in Optical Communications* (Clarendon, Oxford, 1995).

[3] W. Krolikowski, B. Luther-Davies, C. Denz, and T. Tschudi, Opt. Lett. **23**, 97 (1998).

[4] C. Anastassiou, M. Segev, K. Steiglitz, J. A. Giordmaine, M. Mitchell, M. F. Shih, S. Lan, and J. Martin, Phys. Rev. Lett. **83**, 2332 (1999).

[5] Z. Chen, M. Acks, E. A. Ostrovskaya, and Y. S. Kivshar, Opt. Lett. **25**, 417 (2000).

[6] Y. S. Kivshar and G. P. Agrawal, *Optical Solitons: From Fibers to Photonic Crystals* (Academic Press, San Diego, 2003).

[7] T. Dohnal and A. B. Aceves, Stud. Appl. Math. **115**, 209 (2005).

[8] S. P. Yukon and N. C. H. Lin, IEEE Trans. Magn. **27**, 2736 (1991).

[9] V. I. Karpman and V. V. Solov'ev, Physica D **3**, 142 (1981).

[10] V. S. Gerdjikov, D. J. Kaup, I. M. Uzunov, and E. G. Evstatiev, Phys. Rev. Lett. **77**, 3943 (1996).

[11] V. S. Gerdjikov, E. V. Doktorov, and J. Yang, Phys. Rev. E **64**, 056617 (2001).

[12] J. Yang, Phys. Rev. E **65**, 036606 (2002).

[13] M. J. Ablowitz, M. D. Kruskal, and J. F. Ladik, SIAM J. Appl. Math. **36**, 428 (1979).

[14] D. K. Campbell, J. S. Schonfeld, and C. A. Wingate, Physica D **9**, 1 (1983).

[15] M. Peyrard and D. K. Campbell, Physica D **9**, 33 (1983).

[16] D. K. Campbell and M. Peyrard, Physica D **18**, 47 (1986).

[17] D. K. Campbell, M. Peyrard, and P. Sodano, Physica D **19**, 165 (1986).

[18] P. Anninos, S. Oliveira, and R. A. Matzner, Phys. Rev. D **44**, 1147 (1991).

[19] T. I. Belova and A. E. Kudryavtsev, Phys. Usp. **40**, 359 (1997).

[20] Y. S. Kivshar, Fei Zhang, and L. Vázquez, Phys. Rev. Lett. **67**, 1177 (1991).

[21] Fei Zhang, Y. S. Kivshar, and L. Váquez, Phys. Rev. A **45**, 6019 (1992).

[22] Z. Fei, Y. S. Kivshar, and L. Váquez, Phys. Rev. A **46**, 5214 (1992).

[23] J. Yang and Y. Tan, Phys. Rev. Lett. **85**, 3624 (2000).

[24] J. Yang and Y. Tan, Phys. Lett. A **280**, 129 (2001).

[25] Y. Tan and J. Yang, Phys. Rev. E **64**, 056616 (2001).

[26] S. V. Dmitriev, Yu. S. Kivshar, and T. Shigenari, Phys. Rev. E **64**, 056613 (2001).

[27] S. V. Dmitriev and T. Shigenari, Chaos **12**, 324 (2002).

[28] R. H. Goodman and R. Haberman, Physica D **195**, 303 (2004).

[29] R. H. Goodman and R. Haberman, Phys. Rev. E **71**, 056605 (2005).

[30] R. H. Goodman and R. Haberman, SIAM J. Appl. Dyn. Syst. **4**, 1195 (2005).

[31] T. Ueda and W. L. Kath, Phys. Rev. A **42**, 563 (1990).

[32] A. S. Kovalev and A. M. Kosevich, Fiz. Nizk. Temp. **2**, 913 (1976).

[33] N. G. Vakhitov and A. A. Kolokolov, Izv. Vyssh. Uchebn. Zaved., Radiofiz. **16**, 1020 (1973) [Radiophys. Quantum Electron. **16**, 783 (1973)].

[34] I. V. Barashenkov and V. G. Makhankov, Phys. Lett. A **128**, 52 (1988).

[35] K. A. Gorshkov and L. A. Ostrovsky, Physica D **3**, 428 (1981).

[36] J. Yang, Phys. Rev. E **64**, 026607 (2001).

[37] J. Yang, and D. J. Kaup, SIAM J. Appl. Math. **60**, 967 (2000).

[38] N. K. Efremidis, S. Sears, D. N. Christodoulides, J. W. Fleischer, and M. Segev, Phys. Rev. E **66**, 046602 (2002).